CZECH TECHNICAL
UNIVERSITY
IN PRAGUE

F3

Faculty of Electrical Engineering
Department of Cybernetics

Master's Thesis

Estimation of the Laser Beam Parameters

Bc. Anna Žigajkova

Prague, May 2022
Supervisor Ing. Pavel Krsek, Ph.D.

MASTER'S THESIS ASSIGNMENT

I. Personal and study details

Student's name: **Žigajkova Anna** Personal ID number: **474399**

Faculty / Institute: **Faculty of Electrical Engineering**

Department / Institute: **Department of Cybernetics**

Study program: **Cybernetics and Robotics**

Branch of study: **Cybernetics and Robotics**

II. Master's thesis details

Master's thesis title in English:

Estimation of the Laser Beam Parameters

Master's thesis title in Czech:

Určení parametrů laserového paprsku

Guidelines:

1. Study the geometry of the laser beam emitted by a semiconductor laser module with a lens.
2. Propose and implement algorithms for the estimation of parameters of the laser beam, which is the output of the laser module.
3. Test developed algorithms on real data and analyze the results.
4. Write proper documentation.

Bibliography / sources:

[1] Y. Cai, Q. Lin. The elliptical Hermite–Gaussian beam and its propagation through paraxial systems. Optics Communications. Vol. 207, Issues 1–6, 139-147, Elsevier 2002.
[2] Z. Meia, J. Gua, D. Zhao. The elliptical Laguerre–Gaussian beam and its propagation. Optik 118(1):9-12, Elsevier 2006

Name and workplace of master's thesis supervisor:

Ing. Pavel Krsek, Ph.D. Robotic Perception CIIRC

Name and workplace of second master's thesis supervisor or consultant:

Date of master's thesis assignment: **10.01.2022** Deadline for master's thesis submission: **20.05.2022**

Assignment valid until: **30.09.2023**

Ing. Pavel Krsek, Ph.D.	prof. Ing. Tomáš Svoboda, Ph.D.	prof. Mgr. Petr Páta, Ph.D.
Supervisor's signature	Head of department's signature	Dean's signature

III. Assignment receipt

The student acknowledges that the master's thesis is an individual work. The student must produce her thesis without the assistance of others, with the exception of provided consultations. Within the master's thesis, the author must state the names of consultants and include a list of references.

. | Date of assignment receipt | Student's signature

© ČVUT v Praze, Design: ČVUT v Praze, VIC

Acknowledgement / Declaration

I thereby would like to thank my supervisor, Ing. Pavel Krsek, Ph.D., for his guidance and patience.

I declare that the presented work was developed independently and that I have listed all sources of information used within it in accordance with the methodical instructions for observing the ethical principles in the preparation of university theses.

In Prague on 20.05.2022

.....

Abstrakt / Abstract

Tato práce se zabývá určením pozice ohniskového bodu laserového paprsku a jeho úhlu dopadu na čočku kamery. Parametry paprsku jsou určeny ze sekvence snímku, které odpovídají intenzitě laserového paprsku v rovině kolmé na směr šíření v jednotlivých řezech.

Paprsek je v každém snímku aproximován dvou-dimenzionální Gaussovskou funkcí. Poté je určen ohniskový bod z nalezených parametrů. Úhel dopadu paprsku je dopočítán z průběhu pozic středů Gaussovských funkcí vzhledem k polohám jednotlivých řezů.

Navržené algoritmy poskytují stabilní výsledky, a jsou schopné nalézt pozici ohniskového bodu s odhadovanou přesnosti setiny milimetru z poskytnutých dat. V nejbližší době budou nasazeny na pracoviště pro ověření kvality zapouzdřených laserových diod. Pro potřeby vyhodnocení obsluhou, jsou výsledky graficky vizualizovány.

Klíčová slova: laserový paprsek, odhad ohniskového bodu, úhel dopadu, šíření laserového paprsku.

This work aims to implement and experimentally verify an algorithm for finding the focal point of the laser beam and its inclination angle to the camera lens. The parameters are estimated from a sequence of images of the beam's slices. The images are captured perpendicularly to the propagation direction at different distances from the laser source.

In each image, the laser beam's irradiance is approximated by the two-dimensional Gaussian function. As the next step, a beam's waist location is localized. The waist is said to correspond to the laser beam's focal point. The inclination angle is computed by evaluating the Gaussians' function centers in regard to the camera position at the time of capturing the images.

The designed algorithms provide satisfactory and reliable results. The precision of the focal point position estimation in our datasets is evaluated to 0.01 mm for the provided datasets. The algorithm will be deployed at the quality control workstation that was previously manually operated. The output of the algorithm is visualized for the workplace operators.

Keywords: laser beam, beam waist, focal point estimation, laser beam propagation, inclination angle.

Contents

List of abbreviations

CCD	■	Charge-coupled device
CIIRC	■	Czech Institute of Informatics, Robotics and Cybernetics
CMOS	■	Complementary metal–oxide–semiconductor
FWHM	■	Full Width Half Maximum
InGaAs	■	Indium Gallium Arsenide
LSQ	■	Least squares (method)
ND	■	Neutral-density (filter)
NIR	■	Near Infra Red
PSF	■	Point Spread Function
ROIC	■	Readout integrated circuit
TEM	■	Transverse Electric and Magnetic (laser mode)

Chapter 1
Introduction

This work was created as a part of a development project of laboratory equipment. The project was realized by an external company in cooperation with the Czech Institute of Informatics, Robotics, and Cybernetics (*CIIRC*). The company specializes in developing and manufacturing optoelectronic microsystems for various applications. The project aims to develop a measuring device used as a quality checkpoint of encapsulated laser diodes fitted with a lens (*micro-module*). The device should measure the focal point and the inclination angle of the laser beam emitted by the micro-module.

The micro-module is intended to be used for fiber-optic communications. Therefore, the parameters of the emitted laser beam are determined by the application of the module. The angle at which the laser beam is emitted is between two and nine degrees, and the focal point is located between 2-10 mm from the laser source.

The main task of this work was to design an automated algorithm for laser beam parameter estimation. The algorithm should be versatile and not depend on individual focal distances of measured micro-modules or their irradiance.

This chapter introduces the micro-module, the measuring setup, the measuring procedure, and the coordinate system used in this thesis. Chapter 2 provides an insight into a laser beam's propagation in optical systems. Chapter 3 is dedicated to the proposed algorithms. Chapter 4 discusses the cameras used in the measuring device. Experiments and the results are summarized in Chapter 5. In the end, the conclusion is in Chapter 6.

1.1 Micro-module

The laser micro-modules measured during this project are composed of optoelectronic parts. A cross-section of the micro-module is shown in Fig. 1.1. It consists of a laser source, a detection diode, a mirror, and a lens. All the components are fitted on the surface of a silicon wafer of approximately 1×1.5 mm in size. The laser source is a Fabry-Perot cavity laser that emits light parallel to the wafer. The beam is then reflected by the mirror in a roughly perpendicular direction and travels through a focusing lens placed in its path. The detection diode provides feedback that allows measuring the delay in the optoelectronic system.

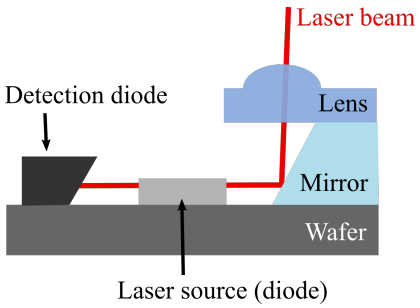

Figure 1.1. A schematic of a micro-module.

The laser beam emitted by a laser source has a focal point, denoted by its manufacturer. The focal point of the laser diode used in this work is set to be 2 mm from the laser source. This number will not correspond to the values measured by the measuring device. It is caused by choosing a different origin point than that originating in the laser source. The referenced plane for the measured focal point in our setup is said to be on the surface of the fitted lens, which under normal circumstances causes an offset of approximately 0.5 mm from the manufacturer's values.

1.2 Measuring device setup

The measuring device is shown in Fig. 1.2 a). A micro-module holder, which keeps the module aligned, is located on a two-stage moving table. The micro-module emits a laser beam directed at the camera lens. In the optical path, the intensity of emitted light must be reduced by a neutral density filter (*ND*, a filter designed to absorb lights of all visible wavelengths equally) or a set of filters. The camera captures images of the laser beam at different propagation distances. This is done by moving the camera on the positioning axis (z') that has been newly motorized.

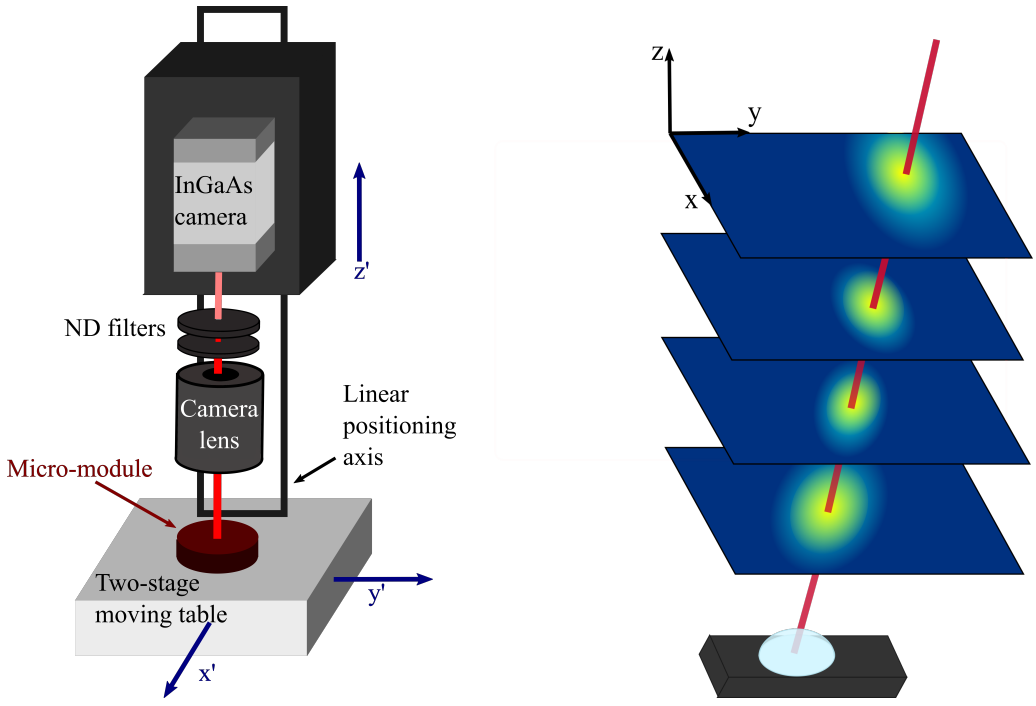

a) Camera setup

b) Laser image capturing

Figure 1.2. Schematic of imaging equipment setup and image capturing procedure. The laser diode emits a laser beam to the camera lens at a slight angle from a perpendicular direction. An ND filter (or set of filters) reduces the beam's irradiance. The filters are placed between the camera lens and the InGaAs camera. This is done due to the technical restrictions of the filter's mounting.

1.3 Measuring procedure

The original workflow at the measuring workplace has involved a considerable workload of an experienced operator. The focal point position is measured from the lens fitted on the laser emitter. The lens position is set to the position when the projected image of the lens is in focus. This step is required to acquire the correct laser focal point position. The operator used to track the real-time images of the laser beam as he adjusted the camera's linear positioning axis. Typical images captured during the measuring procedure are shown in Fig. 1.4. In cases when the images were overexposed, a different ND filter is placed in the camera setup, or the source current is lowered to the diode.

The deciding factor of the laser beam's focal point position was not a single parameter. A compromise between the image sharpness and the highest intensity gain sampled by the camera was required. This procedure heavily depends on the operator's ability to estimate these two properties. The client firm reports that the error rate of the human factor made it possible to determine the beam's focal point position to an accuracy of tenths of a millimeter. Furthermore, the evaluation of one diode could vary among operators.

One of the tasks that were set during the workflow optimization was to limit operator's workload. The automatic solution will also lower the probability of human error in each step. It is intended that the workflow procedure at the new measuring workstation will have these steps

1) Operator places micro-module onto the moving table. As per specification, changes the ND filters (if needed) and powers up the tested micro-module with the specified supply current.
2) Operator calibrates the origin of the z axis to be at the position of the lens in the micro-module.
3) As the motorized linear positioning axis moves the camera, it automatically acquires images of laser beam throughout the anticipated focal point position region.
4) A laser beam's mathematical model is fitted to each image.
5) The parameters fitted to individual images are extracted, and an algorithm estimates a focal point and the inclination angle of the beam.

The contribution of this thesis should be the design of two algorithms. One will fit a laser beam mathematical model to every captured image. The second one will estimate the beam's focal position and its inclination angle to the camera.

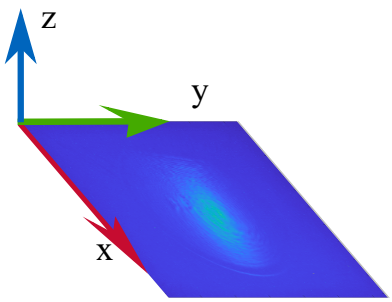

Figure 1.3. Used coordinate system. Picture represents the lens image to which the origin is callibrated.

1.4 Coordinate system

We introduce a coordinate system shown in Fig. 1.2 b) for our experiments. The x, y axes are perpendicular to the optical path of the camera. In practice, they are chosen according to the image processing convention, where x-axis corresponds to the image's rows, and y-axis corresponds to the image's columns, see Fig. 1.3. The origin is set to be in the top left-hand corner.

Axis z is perpendicular to both previous axes, and its orientation is set to be from the laser diode to the camera lens. Practically, the origin of the axis z is set to a position where the edge of the lens is focused in the picture, as shown in Fig. 1.4 a). The laser beam's propagation axis is deviated from the z axis by an approximate angle between 2-9 degrees, as mentioned above. Therefore, as can be seen in Fig. 1.2 b), it causes the laser beam's projection to the image plane to change its location across the captured sequence.

In the theoretical description of a laser beam, we will use a similar coordinate system. The axis z is identical to the propagation axis of the laser beam. The x, y axes are perpendicular and parameterize a laser beam's cross-section. The coordinate system's origin is usually placed at the laser beam's focal point position.

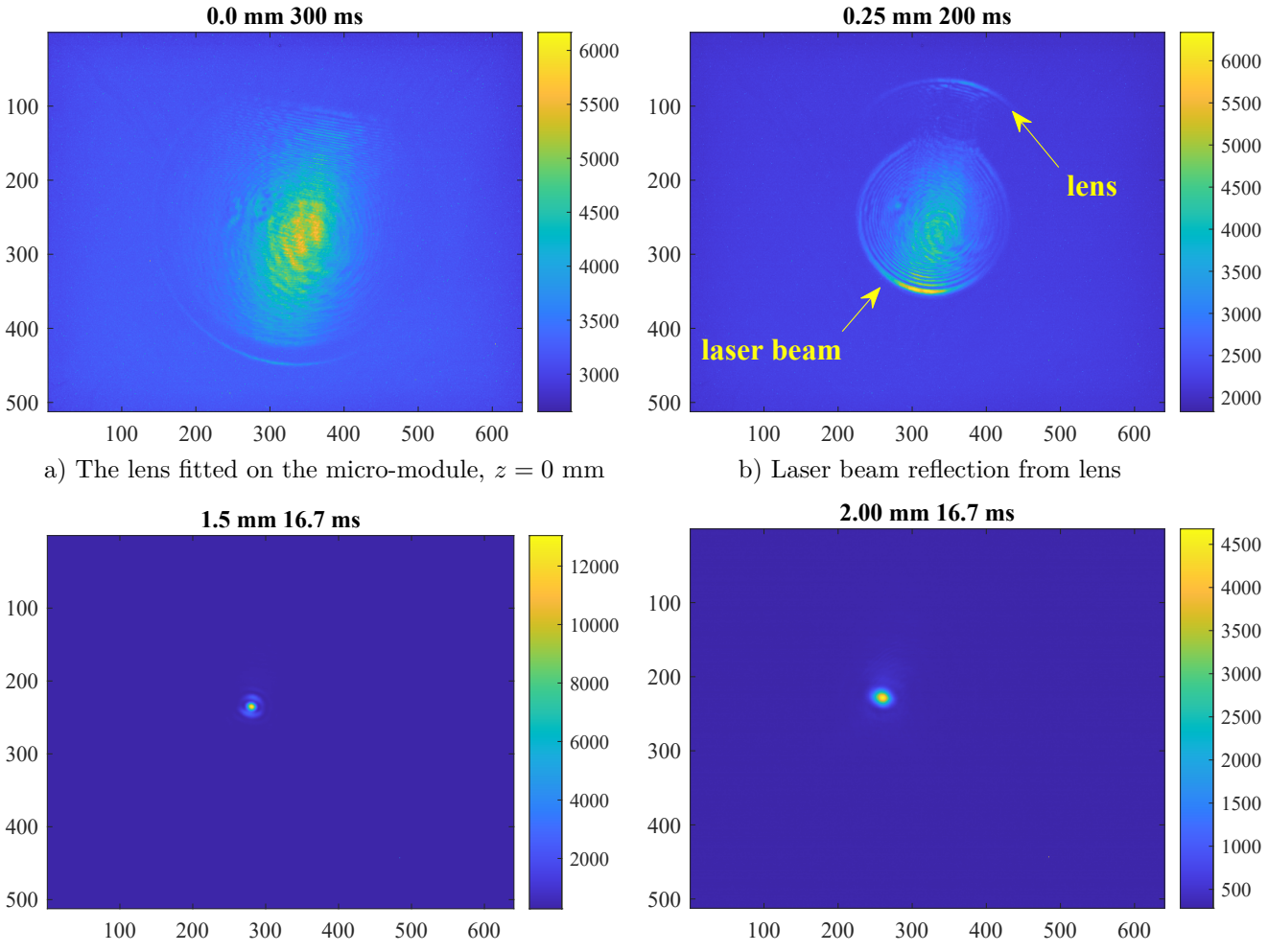

a) The lens fitted on the micro-module, $z = 0$ mm

b) Laser beam reflection from lens

c) Laser beam at focal point

d) Laser beam beyond focal point

Figure 1.4. Examples of images in captured datasets.

Chapter 2
Lasers

In this work, the designed algorithm should approximate laser beam parameters. Therefore, it is convenient to discuss what a laser is and its essential properties. The basic principles are described based on [1].

Word laser is an acronym that stands for *light amplification by stimulated emission of radiation*. The stimulated emission amplifies light in the laser. Still, the lasers prevalent in today's applications should be referred to as oscillators because they generate a beam on their own rather than amplifying the light from an outside source. Laser performance depends strongly on the materials from which they are made. In 1960 Theodore Mainman used a photograph flash-lamp to excite a crystal of synthetic ruby to emit pulses of red light. The chromium atoms in the ruby rod were excited to a higher energy level by a bright pulse of visible light until some of them spontaneously released their energy as red light and dropped to a lower energy level. A silver film coated on the ends of the rod reflected the photons back into the ruby, where they stimulated other excited chromium atoms to emit identical photons in the same direction, amplifying the light. Ruby laser beam gets its color from its chromium atoms, which have absorption bands in the blue and green regions of the light spectrum.

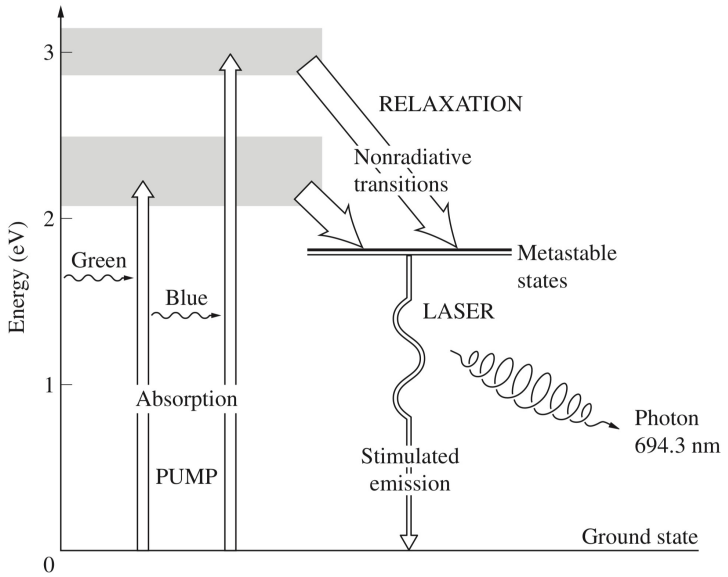

Figure 2.1. Ruby laser energy levels. Adopted from [2], page 621.

For the stimulated emission to occur, a *population inversion*, an excess of atoms in the higher energy level, is needed. Under normal circumstances, most atoms tend to be in their lowest possible energy level, with only a few in higher energy states. This condition is called *thermodynamic equilibrium*. In that case, a photon spontaneously emitted by an atom in the upper state is more likely to encounter an atom in the ground state that will absorb it rather than encountering another atom at a higher level than

it can stimulate to emit another. Therefore no laser action will occur. Real atoms are far more complex than the provided example. They tend to have many more energy levels and possible transitions. Population inversions can occur on two or more different transitions simultaneously, but generally, only one can oscillate at a time.

The laser diodes have reflective surfaces on opposite edges of the wafer that create optical feedback by reflecting light back and forth in the so-called *active medium*. Two mirrors are sufficient in the most basic configuration, with one being semi-transparent. Such design is called a *Fabry-Perot resonator*. The oscillation will start when the gain of the active material compensates for the losses in the laser. This threshold is reached when population inversion reaches the critical value, known as the *critical inversion*. From then on, oscillation will build up from spontaneous emission. The photons emitted along the cavity axis will initiate the amplification process.

The [3] states, that resonators can be divided into two categories, namely, stable resonators and unstable resonators. Under a paraxial approximation, a resonator is said to be *unstable* when an arbitrary ray bouncing back and forth will diverge from the resonator axis. On the contrary, a resonator for which the ray remains bounded will be described as a *stable* resonator.

The light waves resonate if twice the laser cavity length equals an integer multiply of wavelengths. The other waves that do not satisfy this condition are reflected as well, but due to the destructive interference, their gain is lowered in each pass. Therefore this operation can be described as wavelength selection. Stimulated emission amplifies light across a range of wavelengths (called the *gain bandwidth*), and the cavity mirrors reflect them back and forth. The constructive interference selects several wavelengths, which create a set of the *longitudinal modes*. However, their amplitudes are proportional to the gain bandwidth, with the resonant mode having the largest amplitude.

In addition to the longitudinal modes of oscillation, which correspond to standing waves traveling in the propagation direction, transverse modes can also be sustained in laser beams. Since these fields are nearly normal to the propagation axis, these are known as *transverse electric and magnetic* modes (TEM_{ab}). Transverse modes occur because of boundary conditions imposed on the wave by the waveguide (present in an oscillator). The TEM modes can be described by their subscripts. In TEM_{mn} the m and n subscripts are the integer number of transverse nodes in the plane perpendicular to the propagation axis across the emerging beam for the approximations by Hermite-Gaussian functions. The propagation equation of the laser beam can also be written in the cylindrical form in terms of radius (p) and angle (l). The eigenmodes for the equation can be closely approximated by Laguerre-Gaussian functions, denoted by TEM_{pl}. The lowest order mode TEM_{00}, which is often called *Gaussian beam*, is perhaps the most widely used for describing laser beams in optical applications. Its irradiance is an ideal two-dimensional Gaussian function over the beam's cross-section. There are no phase shifts in the electric field across the beam, and it is entirely spatially coherent. TEM_{00} has the smallest divergence, and it can be focused to the smallest-sized spot.

2.1 Types of lasers

Ruby is an example of a *solid-state laser*, in which light-emitting atoms are distributed in a transparent solid. The transparent material is sapphire, and the light-emitting particles are chromium, as was mentioned above. Such transparent solids do not conduct electric current, so the light-emitting atoms must be excited by light from an external source, such as a flashlight or another laser, a process called *optical pumping*.

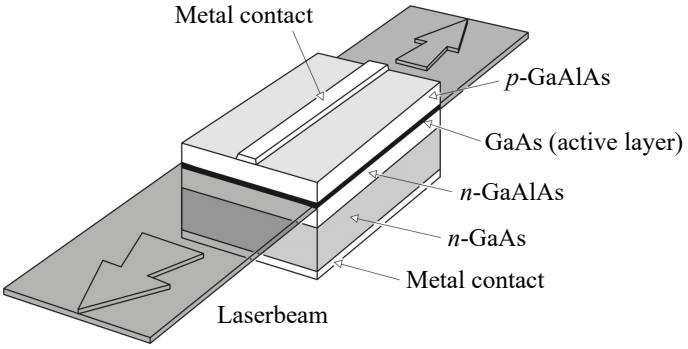

Figure 2.2. Laser diode schematic. Adopted from [2], page 632.

Another broad class of lasers is *gas lasers* in which a light-emitting gas or vapor is confined inside a hollow tube with mirrors at the end. Passing an electric discharge through the gas excites the atoms in states in which they can generate stimulated emission. Most of the lasers in this category have been replaced by semiconductor lasers. However, carbon dioxide lasers are still used in medical and industrial applications.

A third broad class is *semiconductor lasers*, most of them are called laser diodes because they have two electrical terminals, and current flows in only one direction between the terminals to generate stimulated emission inside the semiconductor. These are versatile devices that are nowadays present in all-around applications. As it is the type of laser that is used in our case, it will be discuissed more thoroughly.

2.1.1 Semiconductor lasers and diodes

Semiconductor lasers usually have outputs in the infrared wavelength range, although some existing models can emit in the visible region. The *active medium* is of a semiconductor injection laser is the junction between p and n types of semiconductor materials.

With no voltage applied across the pn junction, charge carriers are uniformly distributed through the crystal material. Near the junction, electrons from n-type material can fall into holes in the p-type material, creating a zone where the charge is distributed unevenly. Usually, no net current flows. Current can flow once the voltage of bandgap energy is exceeded, when it is *forward biased*, by applying a positive voltage to the p-type side and a negative voltage to the n-type side. It attracts the p carriers to the n side of the device and vice versa. They come together at the junction, where the electron and the hole recombine to form electron-hole pair called *exciton*, which releases energy equal to the gap between the conduction and valence bands. It produces a voltage drop at the junction equal to bandgap energy, this area of a diode is often called the *active layer*. A *direct bandgap* is needed to make efficient LEDs and diode lasers that let electrons drop directly from the conduction band to the valence band without changing their momentum. The essential direct-bandgap semiconductors are known as *III-V compounds*, for example, GaAs, InP, and GaN.

In semiconductor laser, the linear cavity is the active stripe in the junction layer, and the flat mirrors are the facets on the chip's edges. A diode laser with a simple cavity can emit light from both facets, shown in Fig. 2.2. In practice, one facet is coated to reflect all or most of the incident light, and the beam emerges from the other facet. In practice, Fabry-Perot diode lasers emit most of their light at one wavelength at any one time but may have sidebands. However, a laser diode may shift to another wavelength (*mode hop*) when its intensity is modulated.

2.2 Laser beam

The practical importance of lasers comes from the unusual properties of light in a laser beam, as described in [3]. The most important properties are summarized in the list below.

- **Monochromacy.** Most lasers are *monochromatic*, but their wavelength generally can be adjusted. The light-emitting material in the laser determines the range of possible wavelengths, and the optics select which wavelengths are emitted by a laser. Since the two-mirror arrangement forms a resonant cavity, oscillations can occur only at the resonance frequencies of that cavity. And only the electromagnetic waves of frequencies $\nu_0 = \frac{E_2 - E_1}{h}$ can be amplified, where h is Planck's constant and E_2, E_1, $(E_2 > E_1)$ are two energy levels of a given atom.
- **Coherency.** The stimulated emission makes laser light *coherent* due to the fact that output photons have the same wavelength and phase as the input photons. The degree of laser coherence differs and can be derived from the wavelengths emitted. The coherence of laser light is both spatial and temporal. Spatial coherence corresponds to the zero difference between the phases at two points. A temporal coherence over time corresponds to the phase of two sampled electric fields at times t and $t + \tau$ difference remaining the same for any time t.
- **Directionality.** Since the active medium is placed in the resonant cavity, the laser beam arrays are *directional*. In the case of the plane-parallel oscillator, only a wave propagating in a direction orthogonal to the mirrors (or very near to it) can be sustained.
- **Divergence.** In the case of perfect spatial coherence, a beam of finite aperture has unavoidable divergence due to diffraction. According to Huygens' principle, as described in [3], the wavefront at some plane behind the screen can be obtained from the superposition of the elementary waves emitted by each aperture point. Finite-size D of the aperture causes the *diffraction limited* beam to have a finite *divergence*

$$\theta_d = \frac{\beta\lambda}{D}, \tag{2.1}$$

  where λ is the wavelength of the beam and factor β is a numerical constant-coefficient whose value depends on the shape of the amplitude distribution and on the definitions of the divergence and the beam diameter. If the wave has only a partial spatial coherence, its divergence will be larger than the minimum value set by diffraction.
- **Continuity.** Some lasers can emit continuous beams, but others are limited to pulses because of their internal physics. The length of laser pulses can vary widely, ranging from milliseconds to femtoseconds. It is achieved by so-called mode-locking. It refers to the locking together of many longitudinal modes in a laser cavity, producing a series of short laser pulses.
- **Brightness.** A laser beam can be described by its *brightness*. It is defined for a given source of electromagnetic waves is defined as the power emitted per unit surface area per unit solid angle. A laser beam of *power* P with a circular cross-section of diameter ω and divergence θ. As stated in [4], the beam brightness B comes to

$$B = \frac{4P}{(\pi\omega\theta)^2}. \tag{2.2}$$

  If beam is diffraction-limited, it has finite divergence, the equation (2.2) becomes

$$B = \frac{2}{(\beta\pi\lambda)^2}P, \tag{2.3}$$

where β is a numerical constant-coefficient as described above. A laser beam of even moderate power (e.g. few milliwatts) has a brightness that is several orders of magnitude greater than that of the brightest conventional sources. This is mainly due to the highly directional properties of the laser beam.

2.2.1 Diffraction

A laser beam as an electromagnetic wave deviates from rectilinear propagation when a portion of a wavefront is obstructed in some way, as described in [2]. The Huygens-Fresnel principle states that every unobstructed point of a wavefront, at a given instant, serves as a source of spherical secondary wavelets with the same frequency as the primary wave. The amplitude of the optical field at any point is the superposition of all the wavelets. Thus, if the wavelength is large compared to the aperture, the waves will spread out at large angles into the region beyond the obstruction.

Three mathematical approaches to describing the diffraction behavior of the beam are presented in [5] volume 2. The diffraction patterns in the near region of a single slit have to be evaluated by direct evaluation of the diffraction integrals. For greater distances under certain conditions, some simplifications may be considered. If the distances are much greater than the wavelength of the laser beam and diffraction angles are small, a Fresnel diffraction approximation is often considered. In the far-field its simplification is the so-called Fraunhofer diffraction. The [5] volume 2. states, that Fraunhofer diffraction integral is proportional to the Fourier transform of the field. The intensity of the Fraunhofer diffraction pattern is equal to the squared magnitude of the field in the aperture plane. Fig. 2.3 shows that the wave amplitude changes significantly in the near field and does not resemble the Gaussian function. The beam is more likely to take that shape in the Fraunhofer distance. Therefore, the laser beam's evaluation is usually divided into examining these two fields separately.

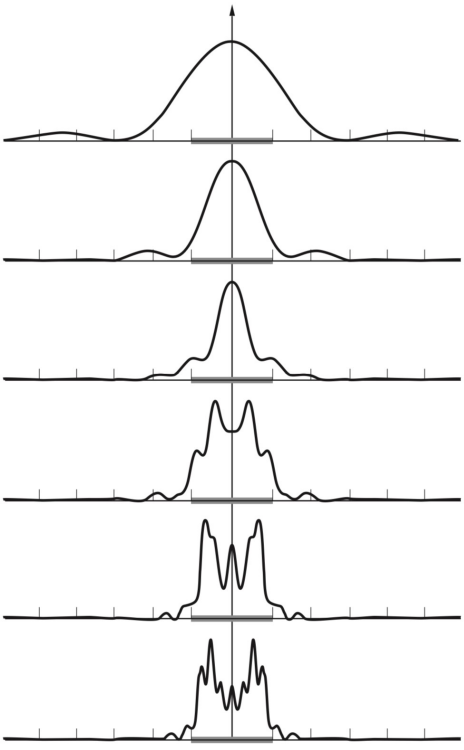

Figure 2.3. A succession of diffraction patterns at increasing distance from a single slit in opaque screen illuminated by plane waves. The diffraction pattern that approximated by the Fresnel is shown at the bottom, Fraunhofer diffraction is shown at the top. The gray band corresponds to the width of the slit. Image adopted from [2], p. 461.

2.2.2 Stigmatic Gaussian beam

A Gaussian beam (TEM_{00}) is the fundamental solution to the paraxial wave equation, as derived in [6] p. 54-57 from Maxwell's equations. The beam's angular divergence is the smallest, and a lens can focus it down to the smallest-sized spot. The amplitude in the TEM_{00} mode is inhomogeneous. For convenience, the laser beam's propagation axis is often regarded as the z axis, see Fig. 2.4.

A stigmatic model of the Gaussian beam is the simplest. It assumes that the beam has a circular irradiance pattern (rotationaly symetric) in the cross-section perpendicular to the propagation axis. Moreover, it is said to have a spherical or a flat wavefront at every point of its propagation distance. As stated in [7] this description is commonly used in laser inferometer simmulations.

For a monochromatic beam, propagating in the z direction with the wavelength λ, the complex electric field amplitude (phasor) as described in [8] is:

$$E(r,z) = \frac{E_0\,\omega_0}{\omega(z)} \cdot \exp\left(-\frac{r^2}{\omega^2(z)} + i\left[kz - \arctan\left(\frac{z}{z_R}\right) + \frac{kr^2}{2R(z)}\right]\right), \tag{2.4}$$

where $|E_0|$ is the peak amplitude and ω_0 is the beam radius at the beam waist, and $k = \frac{2\pi}{\lambda}$ is the *wavenumber*. The parameter r is the radial coordinate of a wavefront point in the plane perpendicular to the propagation axis. The z_R is Rayleight length, and the radius of curvature $R(z)$ of the wavefronts, described below. In each z-plane, the transverse beam profile is again a Gaussian of width $\omega(z)$.

Diameter

A laser beam emitted by a laser diode has some *diameter* that depends on the size of the laser module as well as the output optics. There are different metrics, that address a problem of defining it. The most commonly used is the $1/e^2$ *width*, it corresponds to twice the waist size $\omega(z)$ (as in equation (2.4)). It can be computed as

$$\omega(z) = \omega_0\sqrt{1 + \left(\frac{z}{z_R}\right)^2}, \tag{2.5}$$

where the *waist spot size* ω_0 is the smallest value of the beam's radius at the beam waist position ($z = 0$ for stigmatic Gaussian beams) [3]. Figure 2.4 visualizes the dependency of the beam waist on the position in the propagation direction of z axis. The z_R is the *Reighley range* [3]

$$z_R = \frac{\pi\omega_0^2}{\lambda}. \tag{2.6}$$

Sometimes other measurements are used, such as a so-called *Full Width at Half Maximum* (FWHM, the diameter at half the maximal intensity) or $1/e$ *width*, shown in Fig. 2.5.

Divergence

The diameter varies across the laser beam as it propagates. The divergence of a Gaussian beam can be calculated as in [3]:

$$\theta = \frac{\lambda}{\pi\omega_0}. \tag{2.7}$$

Practically, the divergence of a beam can be measured. The first approach measures the beam spreading angle at considerable distances from the source (in the far field of

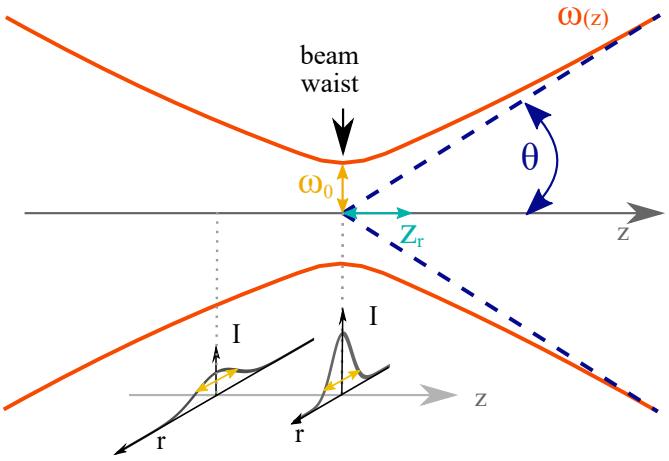

Figure 2.4. Gaussian's beam waist along propagation axis (z-axis).

the laser beam). The second approach is applicable in cases when an abberation-free lens focuses a laser beam down. It measures the beam width ω_f in the focal plane of the lens. The according to [9] the divergence angle is determinedby equation $\theta = w_f/f$, where f is the focal length of the lens.

A *collimated beam* of light is a beam propagating in a homogeneous medium with a low beam divergence so that the beam radius does not undergo significant changes within moderate propagation distances. In the case of Gaussian beams, the article [8] states that the Rayleigh length must be long in comparison to the propagation distance. It is impossible to generate an ideal collimated beam by additional optics since the Gaussian beam always has a finite divergence angle and diverges under free-space propagation.

Radius of curvature

The phase of the laser beam's field distribution is always spherical due to the paraxial approximation. As stated in [5] vol. 2 its dependence on the propagation distance z is given by *radius of curvature* of the wavefront:

$$R(z) = z + \frac{z_R^2}{z}. \tag{2.8}$$

At the beam waist position, the phase is constant, therefore the radius of curvature is infinite. While far away from the waist, the phase function is concentric to the waist position. The minimum radius of curvature is attained at the Rayleigh distance with $R_{min} = 2z_R$.

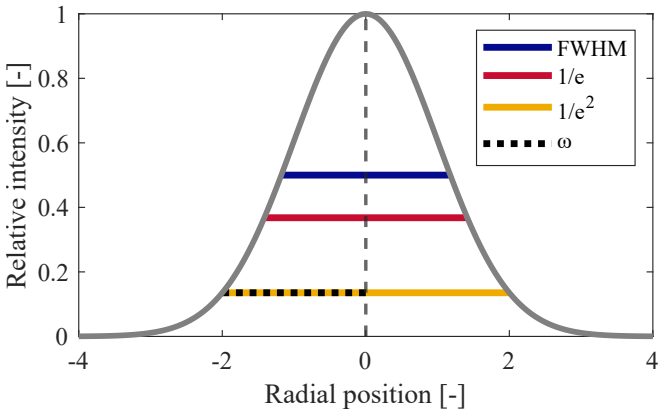

Figure 2.5. Paraxial Gaussian's beam Full Width Half Maximum, $1/e^2$ width and waist.

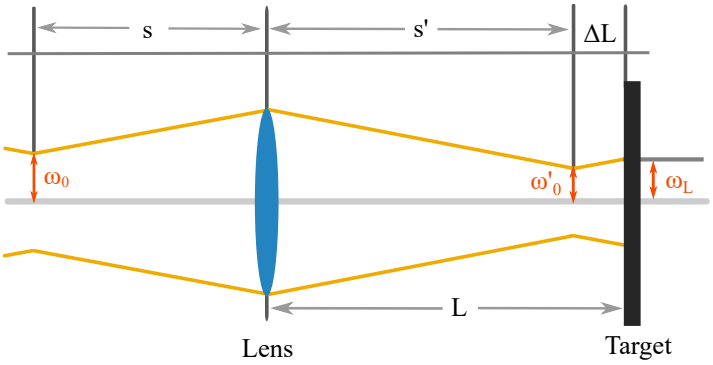

Figure 2.6. Gaussian focal shift. The intensity on the target is maximized, when the beam waist is located before the target.

Gouy phase shift

The Gouy phase shift, as described in [10], is a well-known axial phase shift that a converging light experiences as it passes through its focus in propagation from $-\infty$ to ∞. At position z the Gouy phase of a fundamental Gaussian beam is given by

$$\phi(z) = -\arctan\left(\frac{z}{z_R}\right). \tag{2.9}$$

For a fundamental Gaussian beam, the Gouy phase shift is equal to π. This results in a slightly increased distance between wavefronts than the wavelength defined for a plane wave of the same frequency. There is a similar and more pronounced phase shift for higher-order TEM modes.

Gaussian focal shift

Most semiconductor lasers have beams that spread widely. Therefore an additional optics is constructed to focus the beam into a narrow field. Counterintuitively, the intensity of a focused beam by a lens with focal length f in a target at a fixed distance away from the lens (L, see Fig. 2.6) is not maximized when the waist is located at the target. As described in [11] the intensity on the target is actually maximized when the waist occurs at a location before the target (Fig. 2.6). This phenomenon is known as the Gaussian focal shift. The beam radius at the target, as noted in [11], can be described by the following expression

$$\omega_L = \frac{\omega_0}{z_R}\left(f^2 - 2(|s| - f)(L - f) + \left(\frac{L - f}{\alpha}\right)^2\right), \tag{2.10}$$

where $\alpha = |f|/\sqrt{(s-f)^2 + z_R^2}$ represents the magnification of the beam waist. The variable s represents the distance between the laser's beam waist position and the focusing lens. The differentiation of the equation (2.10) described in [11] shows that the lens focal length resulting in the minimum beam radius, and therefore highest intensity, is at the target.

M^2 factor

The M^2 *factor* (also known as the beam quality factor), described in [11], compares the performance of a real laser beam with that of a diffraction-limited Gaussian beam. It depends on the wavelength λ of the laser beam, on its diffraction angle θ and on the waist spot size ω_0, which should be measured by some available means. The M^2 factor

is defined as

$$M^2 = \frac{\pi\omega_0\theta}{\lambda}. \tag{2.11}$$

Therefore, a factor of 1 corresponds to a diffraction-limited Gaussian beam. Larger values correspond to deviations from an ideal Gaussian beam. Collimated TEM_{00} diode laser beams usually have an M^2 ranging from 1.1 to 1.7. For high-energy multi-mode lasers, the factor can be as high as 25 or 30. In all cases, the M^2 factor affects the characteristics of a laser beam and cannot be neglected in optical designs. In cases when the beam is not paraxial, several M^2 factors are defined (one in each principal axis). The factor of a Hermite-Gaussian TEM_{mn} mode is given by $(2n+1)$ in the x direction and $(2m+1)$ in the y direction.

This factor is crucial because it represents how well a laser beam can be focused for a given divergence. Lower values correspond to smaller spot size, more efficient use of the power within the beam, and a higher potential effective power of the laser.

2.2.3 Orthogonal astigmatic Gaussian beams

Many manufactured lasers produce a beam of an elliptical cross-section. This can be given either by the laser module itself or by the optics fitted to the laser beam's optical path. In such cases, the equation (2.4) can be modified to encompass the descriptions of more general Gaussian beams.

As stated in [7], orthogonal astigmatic Gaussian beams have elliptical irradiance spots and ellipsoidal wavefronts at every point along the propagation. Unlike in the case of a stigmatic Gaussian beam, circular cross-sections are only achieved in few specific points. The orientation of irradiance, represented by a beam spot, coincides with the orientation of wavefronts. Both orientations remain unchanged as the beam propagates through a homogeneous medium. Therefore, such beams have two planes of symmetry, corresponding to the principal semi-axes of the irradiance pattern or the wavefront. The Gaussian beam parameters as were described in section 2.2.2 (beam waist size, divergence, radius of curvature, Gouy phase shift, Gaussian focal shift, M^2 factor) are often defined in both of the principal axes of the orthogonal astigmatic Gaussian beams. In general case, the parameters may differ for each axis.

A complex parameter q that is introduced below is often used in combination with the so-called $ABCD$ matrix to describe the propagation of such Gaussian beams. The parameter q, as described in [3], describes the state of a Gaussian beam at a certain z position:

$$q(z) = \left(\frac{1}{R(z)} - i\frac{\lambda}{\pi\omega^2(z)}\right)^{-1} = z + i \cdot z_R, \tag{2.12}$$

where the radius of curvature $R(z)$ is defined in eq. (2.8), z_R is the Reighley range as defined in eq. (2.6) and $\omega(z)$ is the beam waist as in eq. (2.5). Hence, the electric filed of the elliptical Gaussian beam (as is mentioned in [12]) can be expressed in tensor form as

$$E(\vec{r}) = E_0 \exp\left(-\frac{ik}{2}\vec{r}^2 Q^{-1}\vec{r}\right), \tag{2.13}$$

where E_0 is the peak amplitude, k is the wave number, λ is the laser beam's wavelength, $\vec{r} = [x\ y]^T$ is the position vector in transverse plane. Q^{-1} is the 2×2 complex curvature tensor for the generalized elliptical Gaussian beam given by

$$Q_1^{-1} = \begin{bmatrix} q_{xx}^{-1} & q_{xy}^{-1} \\ q_{xy}^{-1} & q_{yy}^{-1} \end{bmatrix}. \tag{2.14}$$

The individual q_{ij}^{-1} are computed by a generalized form of the equation (2.12) that account for non-axial symmetry. A modified equation is used for the cases, for laser beam's position $z = 0$. The beam waists in individual directions of the principal axes (ω_{0x}, ω_{0y}) and coupled direction (ω_{0xy}) are substited in equation (2.12) and the $1/R(z) = 0$ as the $R(z) \to \infty$ for $z = 0$ as stated in [3]:

$$q_{xx}^{-1} = -\frac{i\lambda}{\pi\omega_{0x}^2}, \qquad q_{yy}^{-1} = -\frac{i\lambda}{\pi\omega_{0y}^2}, \qquad q_{xy}^{-1} = -\frac{i\lambda}{\pi\omega_{0xy}^2}. \tag{2.15}$$

ABCD law

In a paraxial approximation, optical systems behave lineary with reference to the transport of rays or they can be described by a linear collineation. As [5] vol. 1. states, this statement is valid for both the geometrical rays as well as Gaussian beams. In this model, propagation problems can be described in a linear matrix form, which has become common, particularly for Gaussian beams in laser optics.

When a Gaussian beam passes an optical element such as a curved mirror or a lens, this can be described by transforming its parameters with a so-called *ABCD matrix* (the name arises from notation convention as shown in eq. (2.17)). According to [8] the new complex parameter q' is given by:

$$q' = \frac{Aq + B}{Cq + D}, \tag{2.16}$$

where A, B, C, D are constant characteristics of the given optical element and q is from eq. (2.12). For example, the *ABCD* matrix for free space propagation for length L through optical medium with refractive index n is described in [3] as

$$\begin{bmatrix} A & B \\ C & D \end{bmatrix} = \begin{bmatrix} 1 & \frac{L}{n} \\ 0 & 1 \end{bmatrix}. \tag{2.17}$$

When a light ray travels through a thin lens of focal length f the ABCD matrix is modified as follows

$$\begin{bmatrix} A & B \\ C & D \end{bmatrix} = \begin{bmatrix} 1 & 0 \\ -f^{-1} & 1 \end{bmatrix}.$$

The great advantage, that the *ABCD* law has, is that the overall *ABCD* matrix can be obtained by the multiplication of the *ABCD* matrices of the elementary components.

$$\begin{bmatrix} A & B \\ C & D \end{bmatrix} = \begin{bmatrix} A_i & B_i \\ C_i & D_i \end{bmatrix} \cdot \begin{bmatrix} A_{i-1} & B_{i-1} \\ C_{i-1} & D_{i-1} \end{bmatrix} \cdot \ \dots \ \cdot \begin{bmatrix} A_1 & B_1 \\ C_1 & D_1 \end{bmatrix}, \tag{2.18}$$

where i equals to the number of elementary optical components.

The *ABCD* equations are especially useful in describing the propagation of higher order TEM modes as described in [12] and [13]. It provides significant simplification of the propagation equations as the *ABCD* matrix completely characterizes the given optical element within the paraxial ray approximation [3].

2.2.4 Higher TEM modes

For a laser beam traveling in the z-direction, any higher TEM mode solution can be expressed as a combination of Hermite-Gaussian modes for rectangular coordinates or Laguerre-Gaussian modes for cylindrical coordinates, see Fig. 2.7. Both of these solutions are eigenmodes of the paraxial wave equation as described in [6].

Hermite-Gaussian modes

As mentioned above, the fundamental TEM_{00} mode is only one of many transverse modes that can occur in semiconductor lasers. The [3] states that Hermite–Gaussian TEM_{mn} modes are present in lasers with stable resonators and infinite aperture of the output optics. In the article [12] authors present the equation for the higher-order elliptical Gaussian beams in tensor form:

$$E_n(\vec{r},0) = \exp\left(-\frac{ik}{2}\vec{r}^{\,T}Q_e^{-1}\vec{r}\right)\cdot H_n\left[\sqrt{ik\vec{r}^{\,T}Q_h^{-1}\vec{r}}\right], \quad p = 0,\ 1,\ 2,\ \ldots \tag{2.19}$$

where H_n is the n-th order Hermite polynomial. And Q_e^{-1}, Q_h^{-1} are modified complex curvature tensors from equation (2.14).

$$\begin{aligned} Q_e^{-1} &= \begin{bmatrix} q_{xx}^{-1} & 0 \\ 0 & q_{yy}^{-1} \end{bmatrix}, \\ Q_h^{-1} &= \begin{bmatrix} q_{xx}^{-1} & 0 \\ 0 & 0 \end{bmatrix}, \end{aligned} \tag{2.20}$$

with q_{xx}^{-1} and q_{yy}^{-1} being defined as in (2.15).

In article [12] authors substitute equation (2.20) into (2.19) to get the equation describing the TEM_{0n} mode of the Hermite-Gaussian beam:

$$E_n(x,y,0) = \exp\left(-\frac{x^2}{\omega_{0x}^2} - \frac{y^2}{\omega_{0y}^2}\right)\cdot H_n\left[\frac{\sqrt{2}x}{\omega_{0x}}\right], \tag{2.21}$$

where ω_{0x}, ω_{0y}, ω_{0xy} are beam waist sizes in the x, y and coupled direction. Any other $m \neq 0$ Hermite-Gaussian TEM_{mn} mode can be expressed as the product of two elliptical Hermite-Gaussian beams with different order index.

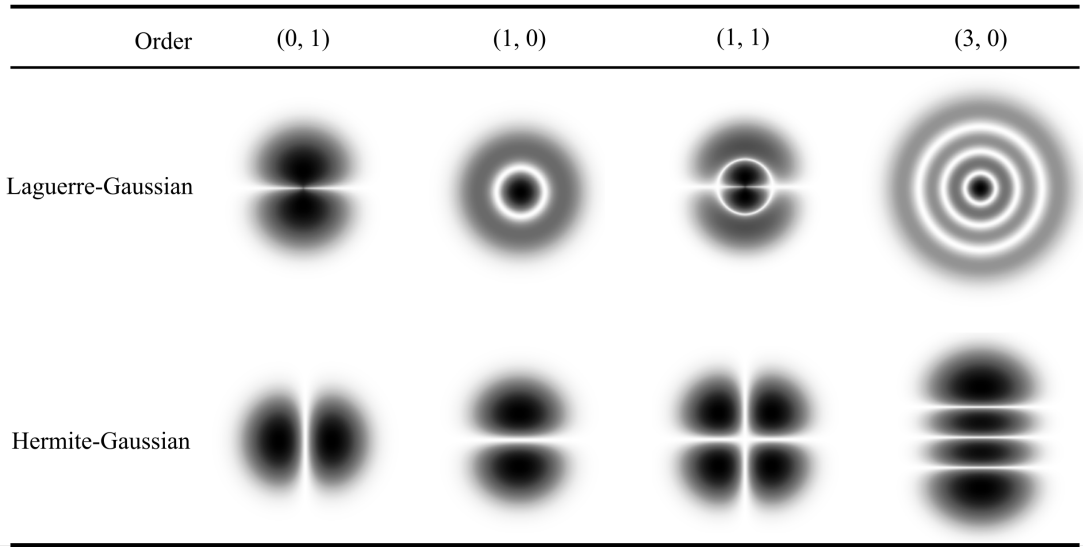

Figure 2.7. Comparison of higher TEM modes' irradiance profiles at $z = 0$.

Laguerre-Gaussian modes

Beam profiles which are circularly symmetric (produced by lasers with cylindrically symmetric cavities) are often described using the Laguerre-Gaussian modal decomposition (TEM_{pl} modes). These beams and their free space propagation is presented in [13]. The electric field of a Laguerre-Gaussian beam at its origin $z = 0$ takes form of

$$E(\vec{r}, 0) = \left(\sqrt{ik\vec{r}^T Q_1^{-1}\vec{r}}\right)^m L_p^l \left[ik\vec{r}^T Q_1^{-1}\vec{r}\right] \cdot \exp\left(-\frac{ik}{2}\vec{r}^T Q_1^{-1}\vec{r}\right), \tag{2.22}$$

where L_p^l denotes the Laguerre polynomial with mode orders p and l.

The intensity distributions of elliptical Laguerre-Gaussian beams are rotationally asymmetric around the z-axis. Moreover, the ellipse cross-section of the beam is tilted from the axes. This angle between the principal axes of the beam spot and the coordinate system can be computed as

$$\alpha_{\text{tilt}} = \frac{1}{2}\arctan\left(\frac{2\,\omega_{0xy}}{\omega_{0x} - \omega_{0y}}\right). \tag{2.23}$$

The equations for propagation of a Laguerre-Gaussian beam through a non-symmetrical optical system were presented together with the simulations in the Optik journal [13].

Gouy phase shift in higher TEM modes

The [10] states that in higher TEM modes, an even stronger Gouy phase shift is also present. For Laguerre–Gaussian TEM_{pl} modes the total phase shift is equal to $(2p + l + 1)\pi$, for Hermite–Gaussian TEM_{mn} modes, it is π multiplied by $1 + n + m$. This change causes the resonance frequencies of higher-order modes in optical resonators to be somewhat higher.

2.3 Propagation through aberrated optical systems

In the case of this thesis, the laser beam is captured by an optical system. The equipment setup used for the imaging was described in Chapter 1, and the camera itself will be discussed in Chapter 4 . The behavior of the laser beam in an optical system is not identical to its free propagation behavior. Moreover, the objective lens fitted on the camera consists of a complex set of focusing optical elements that can produce additional errors in the captured image. Therefore this chapter describes laser beam behavior in a camera by a so-called point spread function (PSF). Which is followed by a discussion of optical aberrations that may be present in our imaging setup.

2.3.1 Point spread function

An important function for describing the propagation of a light point in optical systems is the so-called *Point Spread Function* (PSF) described in [5] vol. 1. PSF describes a single ideal radiant point in the object that emits a spherical wave, which is transversely limited by the imaging system. Hence, we do not observe a pure geometrical-optical point image in the image plane, but a spot instead. The point spread function is broadened as a consequence of the diffraction effects and aberrations. The propagation of the PSF is not identical to the propagation of the stigmatic Gaussian beam, depicted in schematic in Fig. 2.4, as can clearly be seen in Figures 2.8, 2.9.

The article [14] covers the topic of illuminated confocal scanning optical microscopy. They model the illumination source by a Gaussian beam, as is the case for this work.

Fig. 2.8 represents a simulated cross-section in the xz plane of the PSF illumination function. The microscope's objective is focused beyond the Gaussian beam focal point, which resembles our case when the camera lens is focused on the lens fitted on the micro-module. The illumination source is then sampled at different z positions. The Fig. 2.8 differentiates between images by the so-called filling parameter β_G. The parameter defines the ratio of the objective aperture radius to the beam waist radius (the beam waist radius definition used in [14] is the FWHM). The $\beta_G = 0$ defines a constant illumination intensity profile. The perfectly parallel and unfocused beam would have a filling factor $\beta_G = \infty$.

The Fig. 2.8 shows the results of the article [14]. The Fig. 2.9 presents the results of our captured dataset that is closer discussed in Chapters 1 and 5. The filling factor for our dataset as shown in the Fig. 2.9 would be approximately between 0.5 and 1.5. As can be clearly seen, the same phenomenon as described in the article [14] is present in our dataset. However, in our case, the laser beam slightly diverges the camera axis (z-axis) as can be seen on the Row slices.

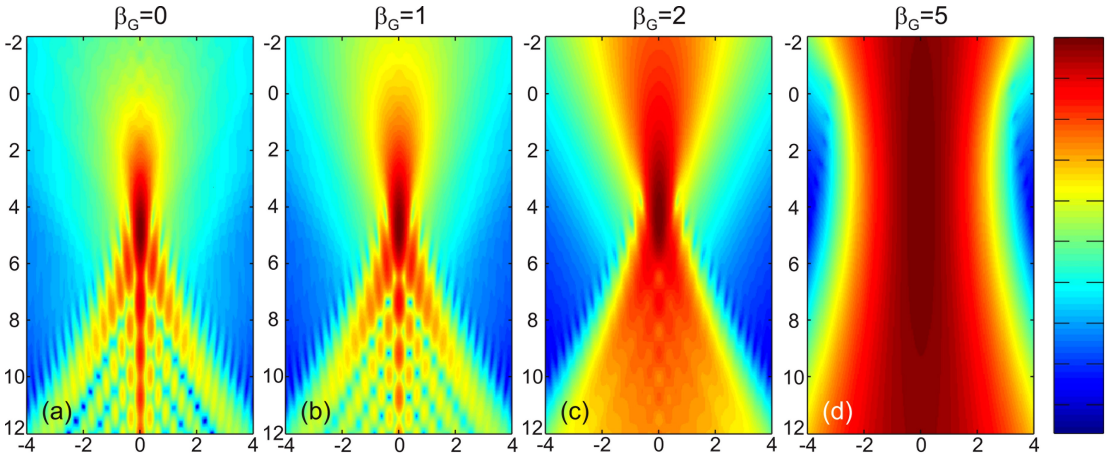

Figure 2.8. Cross sections of the irradiance PSF in confocal microscopy from [14]. The filling parameter β_G defines the ratio of the objective aperture radius to the beam waist radius. Each displayed image is individually scaled between minimum and maximum intensities according to the logarithmic color bar shown on the right. The coordinates are in μm.

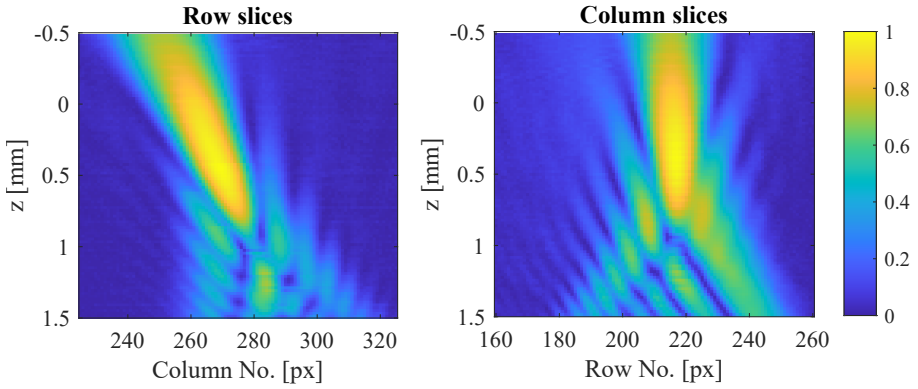

Figure 2.9. Cross-sections of the irradiance profiles extracted from our dataset. The displayed images are scaled between maximum and minimum intensities according to the color bar shown on the right. Row slices correspond to the cross section in the yz plane, column slices correspond to the xz plane.

2.3.2 Optical aberrations

Various properties of an imaging system cause different kinds of optical aberrations. Some of the image imperfections can be analyzed with geometrical optics. However, some require to account for the diffraction theory. The imperfections of optical elements in the optical path can further add aberrations.

The datasets processed in this thesis are monochromatic. A single light source is captured by cameras with infinity-corrected Plan apochromat objective lens, closer discussed in Chapter 4. Therefore, only a selection of optical aberrations relevant to this thesis is described.

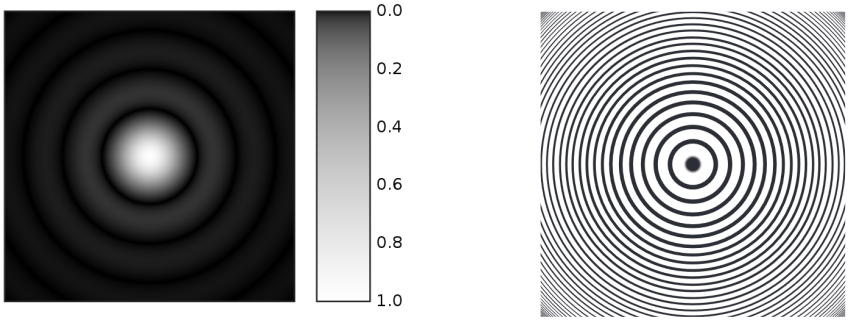

a) Airy disk, adopted from [15]. b) Newton rings, adopted from [2].

Figure 2.10. The Airy pattern caused by Fraunhofer diffraction on circular aperture and the Newton fringes caused by interference.

- **Fraunhofer diffraction** at a circular aperture is an effect detectable in a wide variety of imaging applications. The best-focused spot of light by a perfect lens with a circular aperture is known as the *Airy disk*, described in [2]. The Airy pattern is shown in Fig. 2.10 a). It presents on the imaging surface as a set of concentric disks. The intensity of the pattern diminishes fast from its peak, which is located in the central disk.
- **Interference** can be present in the optical path, even in non-apertured systems. As the [2] states, its source can even be just a reflection from a surface with a different refractive index. Generally, the interference patterns on optical flats manifest as a series of stripes. When a circular lens is present in an optical path, the interference manifests as a set of concentric rings. Contrary to the Airy pattern, it has different irradiance distribution, pattern size, and disk radii, see Fig. 2.10 b).

  The first discussed interference pattern is caused by the fringes of *equal thickness*. They appear due to the presence of a separating medium (lens, dielectric film) with a certain optical thickness parameter in the optical path. These fringes are referred to as the *Fizeau fringes*. A sub-type of these are so-called *Newton rings*, shown in Fig. 2.10 b). It is a pattern that arises when a lens is placed in close proximity to an optical flat, shown in 2.11 b).

  The *fringes of equal inclination* cause the so-called *Haidinger pattern*. It again manifests as a set of concentric rings. However, contrary to the Newton rings, the central region in the Haidinger pattern corresponds to the maximum value. The fringes appear when a light array is reflected by a thick plate, made from an optically denser medium, and is then focused by a lens to the same spot, see Fig. 2.11 a). The equal inclination refers to the fact that the rays emerge at an equal angle from the thick plane. Usually, a combination of both interference patterns is present in images.

- **Spherical Aberrations** are present in most optical lenses, as the spherical surface is the most easily fabricated. As [16] claims, the spherical surface shape, however, is not ideal for imaging. The reason is that the outer parts of the lens are then too strongly curved. This type of aberration can seriously degrade the image quality. This problem can be solved either by using aspheric lenses or by using a combination of lenses designed such that spherical aberrations are well compensated.
- **Astigmatism** is frequently observed when light propagates at a substantial angle to the optical axis. For example, when light rays hit a lens or a curved mirror at large angle, the distance from the lens to the focal point somewhat differs between the vertical and horizontal directions. In the focal plane corresponding to each direction, a point is thus imaged to an elliptical region. The [16] states that the astigmatism of a lens depends on the lens design and cannot be fully corrected for a single lens. It cannot be fully rectified by using a narrow aperture stop, that would preventing light from going through the outer region of a lens. Nevertheless, optical systems that do not exhibit astigmatism can be designed with a suitable combination of lenses.
- **Coma** occurs when light has a substantial angle to the optical axis and propagates throughout the outer regions of a lens. An object point is then imaged to a region with a more or less complicated shape, often somewhat reminiscent of that of a comet. The [16] describes that coma can be reduced with an aperture stop, at the cost of losing image brightness, or with more sophisticated design methods. It is more pronounced for glasses with high magnification.
- **Field curvature** denotes the problem that the focal points of a lens obtained with different incidence angles do not lie on a plane but on a curved surface. This is a phenomenon particularly present in wide-open apertures. Field curvature can make it impossible to adjust the optics for sharp imaging over the entire image plane when using a plane image sensor. The possible solutions for its mitigation are described in [16].

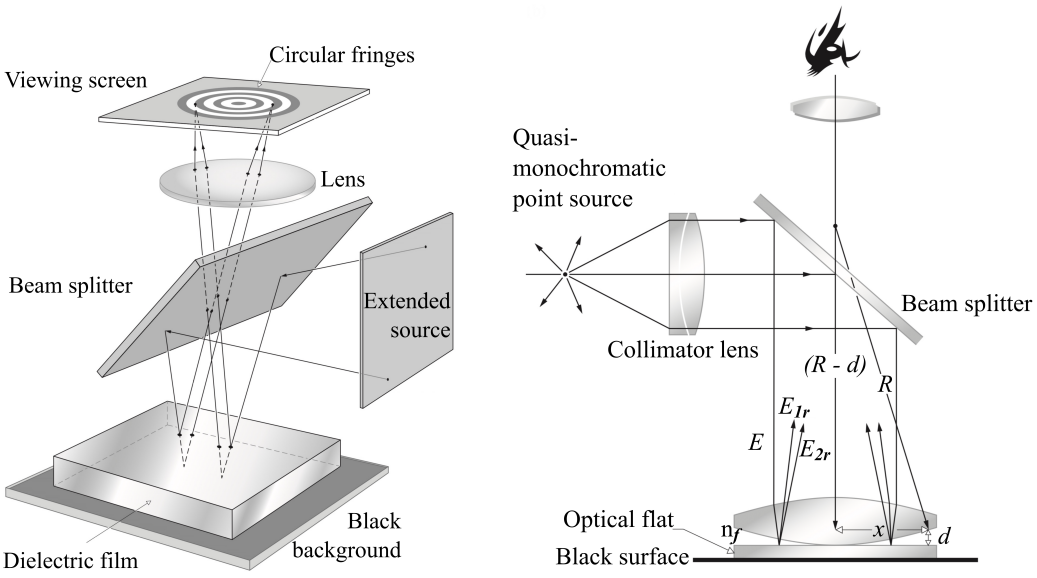

a) Haidinger fringes b) Newton ring

Figure 2.11. Standard setups for observing interference fringes. Adopted from [2], pages 420, 423.

A common method, described in [5] vol. 3., for characterizing any kind of monochromatic aberrations for ray optics is based on a set of mutually orthogonal functions developed by Frits Zernike, known as *Zernike polynomials*. These functions depend on the polar coordinates ρ and ϕ and consist of a radial term $R(r)$ and a term dependent on azimuthal angle ϕ. The azimuthal factor is either $\cos(m\phi)$ or $\sin(m\phi)$, where m is a parameter describing the order. The coefficients obtained by decomposing the wavefront distortions on circular apertures versus position in two dimensions quantify the corresponding types of aberrations. Fig. 2.12 shows the change in the profile of the point spread function for Zernike coefficients factored by c_j in the range between 0 and 0.5λ for the selected aberration of lower order. For aberration coefficients of $c_j \geq 0.2\lambda$, the characteristic form of the PSF allows to distinguish these aberration types. However, for small disturbances, the differences can only be found in the intensity below 10% of the peak value.

All kinds of image aberrations can be minimized with certain design methods for objectives and by operating objectives within reasonable parameter regions e.g. concerning the object distance. Article [16] describes that some kinds of aberrations can be compensated locally. Other kinds of aberrations need to be compensated by inserting different elements in an optical system so that the aberrations approximately cancel each other. It can be rather difficult to compensate for various kinds of aberrations at the same time precisely. Any design change can modify all kinds of aberrations so that one generally cannot solve the different problems one after the other. The actions needed to control the aberrations fall into two categories described in [5] vol. 3. The first one aims at prevention, which is always preferable. The second one tries to compensate for them. Some simple examples are using the aplanatic surfaces for spherical aberration and coma, concentric stop position for astigmatism and distortion, and mirrors for chromatic aberrations. The compensation method minimizes some aberrations by the opposite aberrations at another surface. For distortion, coma, and lateral color, the symmetry principle works perfectly in this sense. For spherical aberration, an aspherical surface may work effectively. The so-called zonal error, which appears as residual aberrations, is a consequence of using the higher-order components that minimize the aberrations.

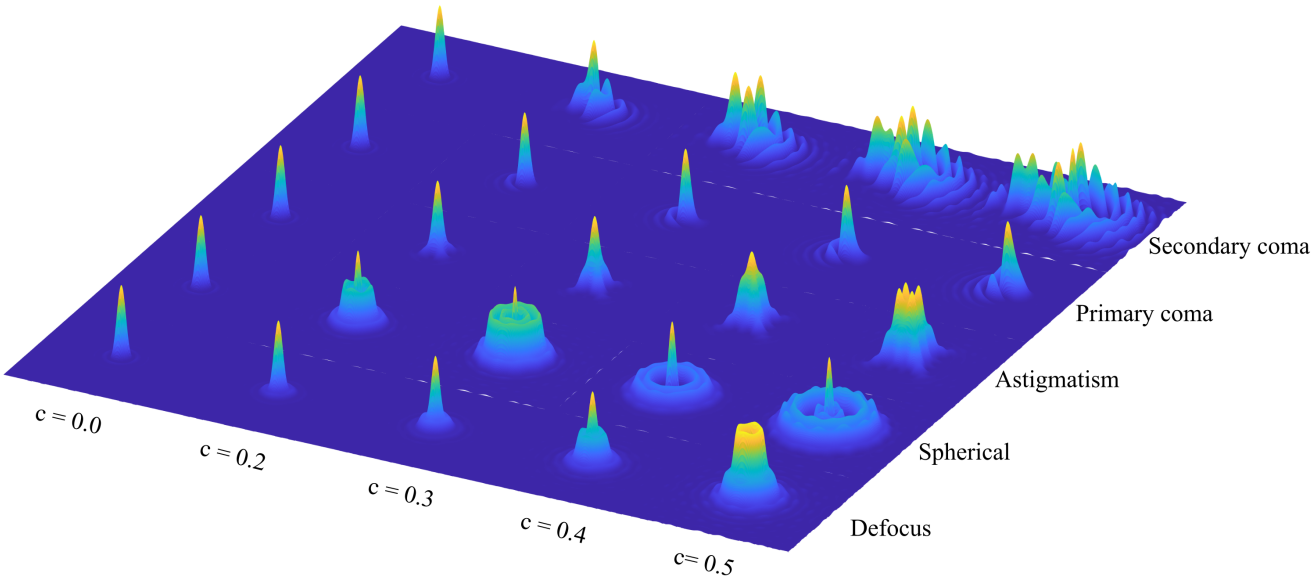

Figure 2.12. Normalized point spread functions for some values of the Zernike coefficients c_j for the lower aberration orders. Generated by modified code from [17].

Chapter 3
Algorithm for beam's parameters estimation

This work aimed to propose, implement, and experimentally verify an algorithm for finding the laser beam's parameters from a sequence of images. The sequence represents the laser beam's slices in the the z axis, as described in section 1.2.

Commercially available lasers are often described in datasheets by their wavelength, beam size, beam divergence, output power, and M^2 factor. For applications where a laser diode's output is coupled into an optical fiber, such parameters as the focal point position and inclination angle become important. Some of these parameters may be measured by using a camera setup.

The international standard [9] describes test methods and principles for measuring beam width, divergence angle, and the M^2 factor. It states that,

1) The optical axis of the measuring system should be coaxial with the measured laser beam.
2) The attenuators or beam-forming optics should be mounted such that the optical axis runs through the geometrical centers.
3) The aperture of the optical system should accommodate the entire cross-section of the laser beam.

Moreover, for pixel-based detector systems, the spatial resolution should be at least 1/20 of the beam width.

The beam width and divergence angle measurement do not require knowing the laser beam's wavelength. Therefore, they can be computed directly from the obtained parameters from the image measurement. Which in theory, could have been measured by the camera present in our measuring device. However, the setup of the measuring equipment used in this work, as described in section 1.2, does not satisfy the criteria 1) and 2). The criterion on the spatial resolution could be fulfilled by using a lens with a magnification of at least 50 times, which is not the case for our datasets as will be discussed in Chapter 4.

The setup for our experiments has been primarily used for determining the focal point position and estimating inclination angle to the camera of the emitted laser beam. Therefore, after consultation with the client firm, we arrived at conclusion that this work will only focus on estimating the focal point position of the laser beam and its inclination angle to the camera. This estimation will require two steps, firstly a parametric description of a single image should be acquired (from laser beam spatial profiling). In the second step, extracted parameters from the fitted functions are processed to estimate the focal point and inclination angle.

3.1 State of the art

Many industrial solutions focus on laser beam spatial profiling, for which plentiful commercial software is available. A standard industry method of measuring the laser beam's profile has been the use of a pinhole technique. The pinhole is used to sample the beam's intensity by mechanically moving an aperture across the beam in a plane orthogonal to the optical axis. In 2007 a modified technique was proposed in article [18]. It used an optical fiber as the pinhole. With the improvement in CCD cameras, the new profilers based on two-dimensional photo-detectors were introduced. In another article, [19], a 3D printed solution for an imaging system was introduced. The authors designed a printable stand for a mobile phone used for imaging and referenced an android app developed by MIT for laser beam imaging. Article [20] authors designed and tested a simple automated setup for measuring the profile and spot size of a Gaussian laser beam. Two standard profiling techniques were implemented, the imaging technique for the CMOS 2D array and the scanning knife-edge-like technique for the single photodiode. Authors claim that the results of the knife-edge-like technique have proved to produce more stable results. However, the CCD camera's beam's waist error, around 1%, is still reasonably small. A comprehensive summary of the available methods is described in [21].

Compared to the number of applications available for laser beam spatial profiling, the possible spectrum of ready-made solutions for the laser focal point estimation from measurement is sparse. Generally, a laser beam waist coincides with the beam's focal point. In [22] an automatic translating beam profiler device of focal spot size and positions is presented. The laser beam is guided perpendicularly to a Pi NoIR CMOS camera. According to the provided results, the beam waist size depends on the propagation axis according to equation (2.5). This is not the case for our datasets, as can be seen in Fig. 3.1. In [23], the author dealt with imaging a laser beam by a CCD camera. The beam waist propagation depicted in the article is similar to our case. Article [24] presents an indirect approach to determining the laser beam focal point position. It is based on an analysis of speckle patterns of a laser beam on a diffusive object. The article states that the strong asymmetry of the beam waist's curve (which, as in our case, cannot be appropriately approximated by a hyperbola), comes from the strong beam divergence and subsequent laser beam size variation on the focusing lens.

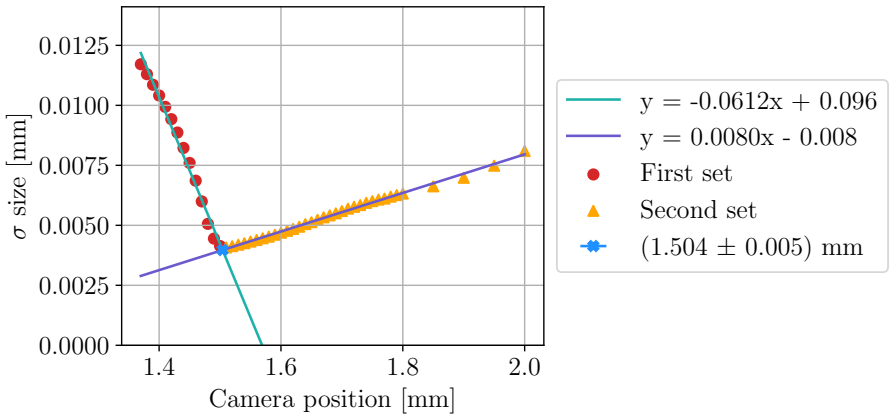

Figure 3.1. Standard deviation parameters of the fitted Gaussians in relation to camera position. For astigmatic Gaussian beam's waist size $\omega(z)$ holds $\omega(z) = 2\sigma(z)$.

3.2 Proposed algorithms

The intensity in the acquired images represents an irradiance cross-section of the Gaussian beam perpendicular to the propagation axis (*z-cut*). The intensity will be approximated by bivariate Gaussian function. Gaussian standard deviations σ_x, σ_y (which correspond to $\omega_x(z)/2$, $\omega_y(z)/2$ for orthogonal astigmatic Gaussian beams in cases when the propagation axis is coaxial to the optical axis of the measuring systems) and Gaussian center position x_0, y_0 will be extracted from the z-cut to determine the focal point position and the inclination angle. The assumptions for the proposed algorithms were

- The laser beam's irradiance profile would be reasonably small for the image size.
- The laser beam is of a TEM_{00} mode. Which is the dominant mode for the Fabry-Perot laser.
- Focal point is located at the laser beam waist. And its location coincide for both principal axes.

A Gaussian function was fitted to each image in the sequence of the laser beam slices. If the Gaussian's curve fit was sufficiently good, the results were processed as follows:

1) Extract sequence of Gaussian's standard deviations σ, which are acquired by bivariate Gaussian distribution fitting (section 3.3)
2) Find the global minimum of the chosen σ sequence. (Corresponds to the position of the focal point in the z-axis). Described in section 3.4 Focal point estimation.
3) Find the beam's inclination angle from the sequence of Gaussian's center coordinates $[x_0, y_0]$ and the camera positions. Described in section 3.5 Beam's angle of inclination estimation.

3.3 Bivariate Gaussian distribution fitting

A bivariate Gaussian function estimates the laser beam irradiance profile for the TEM_{00} mode. We can describe the Gaussian function in the following parametrization:

$$G(x,y) = A\exp\left(-\frac{1}{2}\left[\frac{(x-x_0)^2}{\sigma_X^2} + \frac{(y-y_0)^2}{\sigma_Y^2}\right]\right). \tag{3.1}$$

The coefficient A is the amplitude, x_0, y_0 are the coordinates of the center and σ_X^2 and σ_Y^2 are the variances in x and y directions. This equation is capable of producing only such elliptical Gaussian functions, which axes are identical to these of the used coordinate system. In more general case, the coordinates can be rotated by angle θ around z axis. Such rotation can be represented by a rotation matrix

$$\begin{bmatrix} x_{rot} \\ y_{rot} \end{bmatrix} = \begin{bmatrix} \cos\theta & -\sin\theta \\ \sin\theta & \cos\theta \end{bmatrix} \begin{bmatrix} \hat{x} \\ \hat{y} \end{bmatrix} = \begin{bmatrix} \cos(\theta)\,\hat{x} + \sin(\theta)\,\hat{y} \\ -\sin(\theta)\,\hat{x} + \cos(\theta)\,\hat{y} \end{bmatrix}. \tag{3.2}$$

Where $\hat{x}$ denotes $x - x_0$ likewise the $\hat{y} = y - y_0$. Therefore, if one substitutes the rotated coordinates into equation (3.1) the expression takes form of

$$
\begin{aligned}
G(x,y) &= A\exp\left(-\frac{1}{2}\left[\frac{\cos(\theta)\,\hat{x}+\sin(\theta)\,\hat{y}}{\sigma_x}\right]^2-\frac{1}{2}\left[\frac{-\sin(\theta)\,\hat{x}+\cos(\theta)\,\hat{y}}{\sigma_y}\right]^2\right)\\
&= A\exp\left(-\frac{\cos^2(\theta)\,\hat{x}^2+2\sin(\theta)\cos(\theta)\,\hat{x}\hat{y}+\sin^2(\theta)\,\hat{y}^2}{4\sigma_x^2}\right.\\
&\qquad\left.-\frac{\sin^2(\theta)\,\hat{x}^2-2\sin(\theta)\cos(\theta)\,\hat{x}\hat{y}+\cos^2(\theta)\,\hat{y}^2}{4\sigma_y^2}\right).
\end{aligned}
\tag{3.3}
$$

Offset

Due to the technical properties of the cameras, the base level of pixel read-out is not equal to zero. Therefore, an offset parameter I_0 was introduced into the Gaussian function (3.3) for actual fitting:

$$G^*(x,y) = G(x,y) + I_0. \tag{3.4}$$

One possibility of dealing with the offset is to estimate and subtract that parameter before computing the Gaussian's parameters. However, determining the exact value of that parameter can prove to be quite tricky. Even for imaging a uniform homogeneous background, the pixels' irradiance values differ from each other. In theory, this irregularities should adhere to the Poisson distribution. Which makes it insufficient to sample this parameter only from one value. The exact implementation of this parameter estimation is described in sections 3.3.1 and 3.3.2.

3.3.1 Statistical solution

One possible way of estimating a Gaussian function is to consider each statistical properties of each image. A region of an image is created, that contains only the reasonable neighborhood of Gaussian beam's center. We have decided, to determine the corresponding region by thresholding the pixels intensity levels. After several experiments with our datasets, in which we examined the changes of the computed standard deviations between images in the captured sequence, we have decied to only the pixels, whose values are in the upper 90 % of the maximal intensity will be fitted. Their convex hull will define the fitting region.

In this region covariance matrix is estimated. From definition, the covariance matrix

$$\Sigma = \begin{bmatrix} \sigma_X^2 & \operatorname{cov}(X,Y) \\ \operatorname{cov}(X,Y) & \sigma_Y^2 \end{bmatrix}, \tag{3.5}$$

consists of variance in x and y directions (σ_X^2, σ_Y^2) as well as the covariance in coupled xy direction $cov(X,Y)$, defines the shape of the bivariate normal (Gaussian) distribution as per [25]:

$$p(\vec{x}|\mu,\Sigma) = \frac{1}{2\pi|\Sigma|^{1/2}}\exp\left(-\frac{1}{2}(\vec{x}-\vec{\mu})^T\Sigma^{-1}(\vec{x}-\vec{\mu})\right), \tag{3.6}$$

where $\vec{x} = [x\ y]^T$, and $\vec{\mu} = [x_0\ y_0]^T$.

Ellipsoids of constant density can be computed from the covariance matrix. The eigen-decomposition of the matrix Σ defines the rotation and the scales in individual axes. Its eigenvectors define the principal axes of the constant density ellipse, and the

squares of eigenvalues are proportional to the half-length of the axis as is described in [26]:

$$\sigma_x^2 = \lambda_1, \qquad \sigma_y^2 = \lambda_2,$$
$$\theta = \arctan\left(\frac{v_{1y}}{v_{1x}}\right), \tag{3.7}$$

where parameters λ_1, λ_2 denotes the larger and the smaller eigenvalue extracted from eigenvector decomposition, the $v_1 = [v_{1x},\ v_{1y}]^T$ denotes the eigenvector corresponding to the larger eigenvalue (λ_1).

In the implementation of this algorithm, in the first step, an offset I_0 is estimated, which is then subtracted from the image. Since it is known that cameras contain pixels that measure irradiance inaccurately, it was decided to determine the offset I_0 from a cumulative distribution function of intensities in the captured image. In our datasets, the Gaussian beam's cross-section takes only a lesser part of the image, making it safe to assume that only less than half of the image will contain the beam image. Therefore, it was decided to set a 50% threshold of the cumulative distribution function that will determine the I_0. In the second step, a weighted sample covariance matrix is estimated with normalized reliability weights as described in [27].

$$C = \sum_{i=1}^{N} w_i(\vec{x}_i - \vec{\mu}_w)^T(\vec{x}_i - \vec{\mu}_w), \tag{3.8}$$

where the weighted mean is calculated as $\vec{\mu}_w = \sum_{i=1}^{N} w_i\vec{x}_i$. In our case, the $\vec{x}_i = [x\ y]^T$ correspond to position of each pixel and the w_i is the intensity of corresponding pixel. Lastly, the eigenvectors and the eigenvalues obtained by the eigenvalue decomposition of matrix C are used to compute the unknown variables in eq. (3.7).

This method provides fast results. However, it is prone to be easily influenced by an outlier value that can be present in images due to camera errors. For that reason, an iterative method using the least-squares solution was designed and tested.

3.3.2 Non-linear least squares solution

The Gaussian function equation (3.3) can be written in matrix quadratic form such as

$$G(x,y) = A\exp\left(-\begin{bmatrix} x-x_0 \\ y-y_0 \end{bmatrix}^T \begin{bmatrix} a & b \\ b & c \end{bmatrix} \begin{bmatrix} x-x_0 \\ y-y_0 \end{bmatrix}\right) \tag{3.9}$$
$$= A\exp\left(-\left[a(x-x_0)^2 + 2b(x-x_0)(y-y_0) + c(y-y_0)^2\right]\right). \tag{3.10}$$

We will denote the positive-definite matrix as S

$$S = \begin{bmatrix} a & b \\ b & c \end{bmatrix}. \tag{3.11}$$

The relations between the Gaussian function (eq. (3.3)) and the a, b, c parameters can be easily computed by comparing equations (3.3) and (3.10):

$$a = \frac{\cos^2\theta}{2\sigma_X^2} + \frac{\sin^2\theta}{2\sigma_Y^2}, \qquad b = -\frac{\sin 2\theta}{4\sigma_X^2} + \frac{\sin 2\theta}{4\sigma_Y^2}, \qquad c = \frac{\sin^2\theta}{2\sigma_X^2} + \frac{\cos^2\theta}{2\sigma_Y^2}. \tag{3.12}$$

The algorithm that will fit the equation (3.10) with substituted values from eq. (3.12) will be regarded as *Direct*.

The most problematic parameter to estimate has proven to be the Gaussian's rotation in xy plane, parameterized by the variable θ. Instead of fitting parameters θ, σ_x, σ_y we could fit the parameters a, b, c and then compute Gaussian parameters from the result. If we compare equation (3.6) to (3.1) a simple observation can be made, that

$$\frac{1}{2}\Sigma^{-1} = S. \tag{3.13}$$

From the equation (3.13) the covariance matrix can be obtained as

$$\Sigma = \frac{1}{2ac - 2b^2}\begin{bmatrix} c & -b \\ -b & a \end{bmatrix}. \tag{3.14}$$

However, we do not need to compute the covariance matrix to obtain the Gaussian parameters. If we compute the characteristic polynomial of the S matrix and then substitute for a, b, c from equation (3.12) we get

$$p(\lambda) = \lambda^2 - \lambda(c+a) + ca - b^2 = \frac{(2\lambda\sigma_y^2 - 1)(2\lambda\sigma_x^2 - 1)}{4\sigma_x^2\sigma_y^2}. \tag{3.15}$$

We set $p(\lambda) = 0$ to calculate the eigenvalues. From which follows that we can calculate the variation as

$$\sigma_x^2 = \frac{1}{2\lambda_2},\ \sigma_y^2 = \frac{1}{2\lambda_1}. \tag{3.16}$$

As for the eigenvectors, their directions did not change. Only now, the eigenvector corresponding to the smaller eigenvalue defines the semi-major axis in fitted Gaussian. The angle θ can be computed as in eq. (3.7), but we must use $\vec{v}_2$ instead. This algorithm has proven to converge more easily, and will be regarded as *ABC*.

In both cases, the offset value I_0 is one of variables fitted by the non-linear LSQ algorithms.

Parameters' limits

The non-linear least squares (non-linear *LSQ*) algorithm was used for fitting the Gaussian curve with added offset value $G^*(x, y) = G(x, y) + I_0$, where $G(x, y)$ is defined as in equation (3.10). An algorithm was implemented in the scripting language Python 3.7 using the library scipy. A method used in implementing the non-linear least squares constrained solution is based on Trust Region Reflective method, that is motivated by the process of solving a system of equations, which constitute the first-order optimality condition for a bound-constrained minimization problem. More specifications of the used LSQ algorithm can be found in [28].

The Trust Region Reflective method needs to be provided with the parameter's limits. They were set to:

- x_0, y_0 ..... $\langle$0, image's height$\rangle$, $\langle$0, image's width$\rangle$.
- σ_x, σ_y ..... $\langle$1, image's height/2$\rangle$, $\langle$1, image's width/2$\rangle$.
- θ ..... $\langle 0,\ \pi/2\rangle$.
- A ..... $\langle$minimal pixel value, number of camera's available gray levels$\rangle$.
- I_0 ..... $\langle$minimal pixel value-5, maximal pixel value$\rangle$.

Determination of the Gaussian's center parameter (x_0, y_0) limits is straightforward. We expect it to be in the image. Also, we expect the laser beam to be fully captured by the sensor. Size of the sensor defines the boundaries of thr Gaussian standard deviation parameters (σ_x, σ_y). The angle was set to just the first quadrant as the axes flip could

compensate for it. We expect the Gaussian's offset I_0 to be within the limits defined by minimal pixel value and maximal pixel value in an image. The constant -5 accounts for the discrepancies of the actual Gaussian beam irradiance and the discretized values measured by the camera. The camera's maximal achievable intensity defines the higher limits.

Initial guess

The results were proven to be highly affected by the initial guess of the Gaussian parameters. In the simplest case, the initial guess was set based on the observations of the datasets. This method will be referenced to as the *Max*:

- x_0, y_0 ..... brightest pixel position.
- σ_x, σ_y ..... 10, 10.
- θ ..... 0.
- A ..... difference between the brightest and the darkest pixel.
- I_0 ..... image's lowest intensity value

The number 10 was chosen from studying available datasets for micro-modules fitted with 2 mm diodes. This method of determining the initial guess has proven detrimental for images in which the erroneous pixels values are present, as they skewed the parameters away from the correct Gaussian beam's peak. On top of that this estimate is not ideal in cases, when the θ rotation angle differs significantly from the assumed value. This may produce inaccurate results in some images. Moreover, if a laser diode was used than that to which the σ parameters were designed for, the estimate may be significantly off, which could cause inability of the non-linear LSQ algorithm to converge for several images in the dataset.

Therefore a new method of initial parameters estimation was introduced. An ellipse was fitted to a thresholded image to which a convex hull was applied. This provided a better initial guess of the parameters. The ellipse fitting was implemented using the OpenCV Python module.

Firstly, the image was thresholded by value

$$t = 0.1 \cdot (I_{max} - p_{50\%}) + p_{50\%},$$

where $p_{50\%}$ denotes the 50% percentile of intensities and the I_{max} denotes the highest recorded intensity in the image. Then the connected components in the 8-neighbourhood are found. Lastly, the convex hull of the largest component is found to which an ellipse is fitted in the least-squares sense. The initial guess estimation method *Ellipse* then sets Gaussian's parameters to:

- x_0, y_0 ..... ellipse's center point position.
- σ_x, σ_y ..... half-lengths of the ellipses diagonals.
- θ ..... ellipse's rotation angle.
- A ..... difference between the brightest and the darkest pixel.
- I_0 ..... image's lowest pixel value.

Non-linear LSQ termination criteria

The non-linear LSQ is an iterative method. Several of the deciding criteria can be used for determining the appropriate timing for the algorithm's termination. As described in [28] for the Trust Region Reflective algorithm mentioned above, four termination criteria are checked in each iteration:

- **Maximal number of iterations.** This condition terminates the algorithm if the current iteration number exceeds the maximal number set.
- **Cost function change.** The cost function $F(x)$ is defined as

$$F(x) = \frac{1}{2}\sum_{i=0}^{m}[r(x)]^2, \tag{3.17}$$

  where $r(x)$ is the residual at point x and m represents an m-dimensional fitted function (in our case $m = 2$). The optimization process is stopped when the derivation between iterations of the cost function $F(x)$ is less than the $10^{-8} \cdot F(x)$, and there was an adequate agreement between a local quadratic model and the true model in the last step.
- **Change in the fitted parameters.** This criterion terminates algorithm when difference in the fitted parameters values is less than $10^{-8} \cdot (10^{-8} + |x_{opt}|)$ between iterations, where the x_{opt} is the fitted parameter.
- **Norm of the gradient.** This criterion terminates the algorithm when $|g_{scaled}|_\infty < 10^{-8}$, where g_{scaled} is the value of the gradient of the cost function scaled to account for the presence of the bounds, $|\cdot|_\infty$ denotes the infinity-norm.

If the function reaches the maximal number of iterations it is said that the fitting *failed*. The fit may also fail even if it was terminated by the other two conditions, when the fitted parameters do not have adequate standard deviation error. If either of the standard deviation errors returned by the SciPy's fitting function are greater than the scope of the parameter's limits, it is said that the fit *failed* as well. Such great standard deviation values are caused by the internal implementation of the fitting function. As it may return a covariance matrix with extremely large elements in cases, when the optimization process failed to find an adequate solution.

The value 10^{-8} is the default for the SciPy's fitting algorithm. It need not to be adjusted for our intended use. The maximal iterations number was set to 70, which was chosen empirically. According to the performed experiments it should be suitable for all the images, in which the data that can be approximated by the Gaussian function are present. Further on, only the successful (non-failed) fits are processed.

3.4 Focal point estimation

This work assumed that the laser beam's focal point is located at the beam waist. We suppose that its position corresponds to the global minimum of the larger Gaussian's standard deviation parameters. Fig. 2.4 shows the extracted Gaussian standard deviation parameters form the captured dataset (σ *sequence*). As expected, the σ values are at discrete locations, which would impose, that its global minimum value may not have been represented in a dataset. Moreover, the σ sequence in figure does not resemble a hyperbola, as was described by eq. (2.5). It was decided to approximate the σ sequence by two straight lines, $y = ax + b$. The beam waist (focal point) will be located at the intersection of the lines. The propagation distance determined in this way should be reasonably accurate given provided datasets.

The sequence is sliced at the minimal fitted value. The first half of the σ sequence (*first set*) is fitted by the first line, and then the value of the slice and all of the remaining values (*second set*) are fitted by the second line.

The line parameters a, b were fitted by the linear least-squares method. An unbiased estimate of the fitted line variance can be computed as

$$\sigma_{line}^2 = \frac{1}{n-2}\sum_{i=1}^{n} r_i^2, \tag{3.18}$$

where $r_i = y_i - ax_i - b$ is a residual and n corresponds to the number of fitted points. The variances of the line parameters can be computed as in [25]:

$$\begin{aligned}\sigma_a^2 &= \frac{\sigma_{line}^2}{\sum_{i=1}^{n}(x_i - \bar{x})^2},\\ \sigma_b^2 &= \frac{\sigma_{line}^2 \cdot \sum x_i^2}{n \cdot \sum_{i=1}^{n}(x_i - \bar{x})^2} = \sigma_{line}^2\left(\frac{1}{n} + \frac{\bar{x}^2}{\sum_{i=1}^{n}(x_i - \bar{x})^2}\right).\end{aligned} \tag{3.19}$$

The sample mean is computed as $\bar{x} = 1/n \cdot \sum_{i=1}^{n} x_i$. The coordinates of the intersection point of two fitted lines can be computed as

$$\begin{aligned}x' &= \frac{b_2 - b_1}{a_1 - a_2} = \frac{\Delta b}{-\Delta a},\\ y' &= a_1 x' + b_1.\end{aligned} \tag{3.20}$$

Generally, the parameters a_i and b_i do have dependent uncertainties. Then, the variance of interception abscissa is computed according to the first order propagation of interception variance as in [29]:

$$\begin{aligned}\sigma_{x'}^2 &= \frac{\sigma_{\Delta b}^2 + x'^2\sigma_{\Delta a}^2 + 2x'\mathrm{cov}\,(\Delta a, \Delta b)}{\Delta a^2},\\ \mathrm{cov}\,(\Delta a, \Delta b) &= -\bar{x}_1\sigma_{a_1}^2 - \bar{x}_2\sigma_{a_2}^2,\end{aligned} \tag{3.21}$$

where $\bar{x}_1$ is the mean of the x-values of the first set and the $\bar{x}_2$ is the mean of the x-values of the second set.

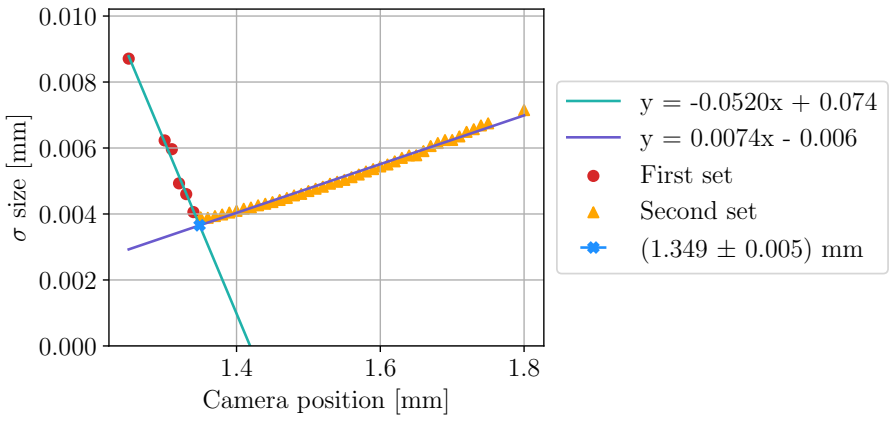

Figure 3.2. Standard deviation parameters of the fitted Gaussians to real dataset in relation to camera position.

In article [29], another method for estimating the standard deviation of the intersection's abscissa deals with confidence intervals instead of statistical uncertainty of the intersection point. The metrics are based on the Student's t-distribution. The bounds of x-coordinate of the intersection point can be computed as the roots of the equation

$$\left[\Delta b^2 - t^2\sigma_{\Delta b}^2\right] + \left[2\Delta a\Delta b - 2t^2\mathrm{cov}\left(\Delta a, \Delta b\right)\right] x' + \left[\Delta a^2 - t^2\sigma_{\Delta a}^2\right] x'^2 = 0. \tag{3.22}$$

The t parameter of the Student's distribution can be adjusted so it corresponds to the variance of the normal distribution. In such cases, the difference in results given the equation (3.21) and (3.22) is minimal. Therefore the equation (3.21) was implemented since it does not require an additional parameter (t) computation.

3.5 Beam's angle of inclination estimation

The laser beam's inclination angle is estimated from a fitted Gaussian centers sequence at different cuts in the z axis. A line is fitted to the data using an algorithm for fitting an n-dimensional plane described in [30] using *singular value decomposition* (SVD).

$$USV^T = [\vec{x} - \bar{x},\ \vec{y} - \bar{y},\ \vec{z} - \bar{z}], \tag{3.23}$$

where $\bar{x}, \bar{y}, \bar{z}$ denotes the values' mean in each corresponding axis. The computed line can be represented in a parametric form as a vector $\vec{v} = [\vec{v}_x, \vec{v}_y, \vec{v}_z]^T$ and a point $p = [\bar{x}, \bar{y}, \bar{z}]^T$. The line vector coordinates of the right singular vector correspond to the largest singular value. The sum of the rest of the squared singular values defines the variance of the fitted line.

The inclination angle for means of visualization is decomposed into two components. One corresponding to the $\pi/2-$elevation and the second one is the azimuth, see Fig. 3.3. The angles are computed as

$$\frac{\pi}{2} - \text{elevation} = \alpha = \arccos \frac{\vec{z} \cdot \vec{v}}{\|\vec{z}\| \cdot \|\vec{v}\|}, \tag{3.24}$$

$$\text{azimuth} = \beta = \arctan \frac{\vec{v}_y}{\vec{v}_x}, \tag{3.25}$$

where $\vec{z} = [0,\ 0,\ 1]^T$. In eq. (3.24) the argument of the numerator is the dot-product of two vectors, and the denominator is the multiply of the norms of the vectors.

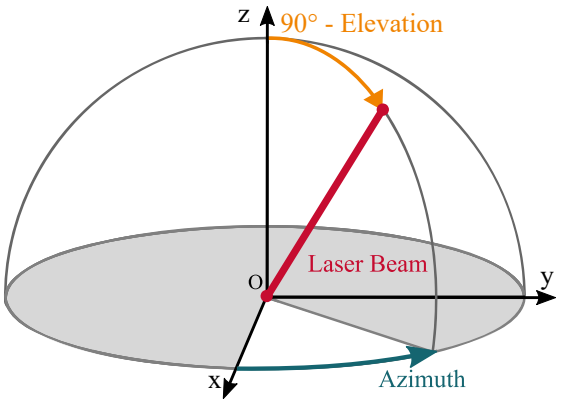

Figure 3.3. A schematic of the laser beam and its projected angle of inclination.

3.6 IOA

An extensive range of camera positions may be used during a measurement. We want to limit the amount of fitted functions during the estimation of the focal point and inclination angle. The laser beam resembles the theoretical Gaussian beam in the region near to its focal point. In the further regions, various optical aberrations that are described in section 2.3 influence significantly the laser beam's cross-section captured in the image. Near the focal point, the laser beam's spot size is significantly reduced, which consequently concentrate its irradiance to the smaller region. It manifests in captured images as higher intensity levels on a smaller number of pixels.

Therefore, we introduce a new parameter that will measure the intensity on per pixel basis under fitted Gaussian function. In its essence, it is a weighted sum of pixels' intensity $I(x, y)$ over Gaussian's elliptical cross-section, which will be regarded as IOA (*Intensity Over Area*). The IOA value depends on Gaussian's standard deviations (eq. (3.3)) and is computed as

$$\mathrm{IOA} = \frac{1}{n} \sum_{(x,y)\in e} I(x, y), \tag{3.26}$$

where n is the number of pixels in an elliptical mask e:

$$e \rightarrow \left(\frac{\Delta x \cos\theta + \Delta y \sin\theta}{\sigma_x} \right)^2 + \left(\frac{-\Delta x \sin\theta + \Delta y \cos\theta}{\sigma_y} \right)^2 \leq 1. \tag{3.27}$$

with $\Delta x = x - x_0$, $\Delta y = y - y_0$. In the case, when the captured sequence contains images of both sides of the focal point position with a reasonable spatial resolution, the important data (regarded as inliers) for focal point estimation would have IOA values larger than 30% of maximal IOA (IOA_{max}) present in the dataset. The threshold was set experimentally.

When different shutter speeds are used, it is necessary to compensate for the different lowest intensity values that camera can produce at different exposure times. The proposed steps for normalization are:

1) Determine the dependency of the dark image intensity (image captured by camera with blocked out illumination, i.e. with a cap on the lens) on camera shutter speed.
2) Approximate the dependency by a function. We expect the dependency to be linear, therefore we estimate a, b parameters in

$$y = a \cdot \text{shutter speed} + b. \tag{3.28}$$

3) Normalize either the whole image in pre-processing, or just the elliptical cross-section in IOA computation by equation (3.29).

$$I_{\text{normalized}}(x, y) = \frac{I(x, y) - b}{\text{shutter speed}}, \tag{3.29}$$

where b is from equation (3.28). And then the normalized pixel intensity is used in eq. (3.26).

Chapter 4
Imaging setup

This chapter discusses cameras used in this project and their properties. The camera one is the remainder of an old equipment setup used until camera two arrived, which was delayed by a chip shortage.

4.1 Cameras

The first half of the datasets was captured using camera HAMAMATSU C14041-10U, referred to as camera one. Later in the project this camera was upgraded to HAMAMATSU C12741-03, referred to as camera two. The main parameters of these cameras can be found in Tab. 4.1. Camera two has twice as many pixels as camera one, doubling its effective scanned area. However, the lower shutter speed limit for the camera two is reduced to only 16.7 ms.

The sensor used in camera two is not specified in the camera's datasheet [31]. The most likely sensor in camera two is HAMAMATSU G13393-0909W . It is parametrically the closest sensor manufactured by HAMAMATSU to the specifications of camera two. An excerpt of sensors parameters is in Appendix B, the whole datasheet is accessible in [32].

Both before mentioned cameras are of type *InGaAs* (Indium Gallium Arsenide). The cameras were chosen due to the wavelength of the tasted lasers. InGaAs area image sensors detect near-infrared light. They have a hybrid structure consisting of a two-dimensional back-illuminated InGaAs photodiode array and a high-gain low-noise CMOS readout integrated circuit (*ROIC*) connected by *In* bumps. A pixel is made up of one InGaAs photodiode element and one ROIC. These cameras are ideal for use in a wide range of applications including internal inspection of silicon wafers and devices, laser beam alignment and evaluation of solar cells, as is noted by the Hamamatsu in [31].

Figure 4.1. HAMAMATSU C12741-03 InGaAs camera. Adopted from [31].

Figure 4.2. M Plan Apo NIR 20X lens. Adopted from [33].

Parameter	Camera one	Camera two	Units
Effective number of pixels	320×256	640×512	px
Pixel size	20×20	20×20	μm
Effective area	6.4×5.12	12.8×10.24	mm
Sensitivity wavelength	$950 - 1700$	$950 - 1700$	nm
Exposure time	$4.6 - 1000$	$16.7 - 1000$	ms
Shutter mode	rolling shuter	rolling shuter	-
A/D converter resolution	14	14	bit

Table 4.1. Excerpt of HAMAMATSU C14041-10U (camera one) and HAMAMATSU G13393-0909W (camera two) parameters. Full list is accessible from [31].

The objective lens used in combination with camera two is an infinity corrected Plan apochromat objective, Fig. 1.4. As stated in [34], an apochromatic objective lens is a chromatic aberration corrected for red, blue and yellow, making it ideal for white light applications. It is optimized for bright light illumination, which makes them highly efficient for in-line illumination applications. The objective lens used in our case is near-infrared wavelength corrected. It is designed so that the image of a workpiece remains focused within the focal depth even when the wavelength used is changed from within the visible range up to the near-infrared (480 to 1800 nm). Its parameters can be found in [33].

4.2 Pixel defects identification

Digital images are prone to different types of pixel errors. Some of the defects may, unfortunately, affect our algorithm. Therefore we need to take them in consideration. A method of classifying such errors is described in [35], where five types are distinguished:

- **Dead pixels** are entirely insensitive and do not respond to incident light. These pixels appear as black or dark spots in images and may manifest due to defects in the underlying hardware.
- **Stuck pixels** exhibit constantly high values. In the case of a 14-bit camera, it would correspond to the value $2^{14} - 1$. In contrast to dead pixels, stuck pixels appear as bright spots. They result from the output transistor's failure, which may get stuck, as in the case of dead pixels.
- **Hot pixels** are caused by extensive dark current. They are persistent and appear at fixed spatial locations in a detector. The extra dark current adds an offset to the pixel's measured charge in such pixels. Since the temperature directly affects the dark current production within a detector, the number of hot pixels increases with increasing temperature. Hot pixels appear as bright spots in uniformly illuminated images.
- **Abnormally Sensitive Pixels**. In an ideal detector, upon exposure to a uniformly illuminated image, the response of all pixels should be almost identical, with minimal variation across the detector. However, all detectors are non-uniform and have pixels that are either more sensitive (*hypersensitive*) or less sensitive (*hyposensitive*) than average. This type of abnormalities may manifest due to the nonuniformity in the detector's readout circuit and the digitalization electronics of individual pixels.
- **Column Defects and Traps**. All the pixels in a single column or multiple columns in a detector can be defective. Such columns are called bad columns. They are usually produced by fabrication faults during the detector manufacturing phase.

A baseline method for studying pixel errors is based on a statistical analysis of dark and bright images. The dark image refers the pictures captured by camera, when no light affects the camera's sensor (e.g. camera lens cap is on). Bright images are captured of a uniform background with the uniform lighting. The pixels should not be overexposed. Since both cameras work at unusual wavelengths, acquiring a bright image has proven challenging. The only available lighting method was a test laser diode, which illuminated only a circular area with non-uniform light density, which limited the ability to identify dead pixels. Therefore the camera tests mainly focused on identifying stuck pixels, hot pixels, column and row defects, and the intensity of the dark images. The intensity of the dark image varies across pictures captured at different shutter speeds. Therefore, in our case this dependency is an essential parameter, because the shutter speed can change during the process of capturing laser beam slices.

4.2.1 Algorithm for identifying erroneous pixels

We acquire a statistically significant number of dark images for the shortest shutter speed intended to be used and the longest shutter speed. The intensities in the captured images should be averaged on per pixel basis (*mean image*) in the regarded two groups, and their variance map (*variance image*) should be determined.

Then, the pixels are evaluated by a criterion that searches for value outliers. An outlier is detected id its value deviates more than 15 times from the standard deviation σ_x from the mean value $\bar{x}$. The $\bar{x}$ and σ_x are computed over all the pixel values for both the mean image and variance image. The inlier interval can be noted as

$$x_{\text{inlier}} \in \langle \bar{x} - 15\sigma_x,\ \bar{x} + 15\sigma_x \rangle. \tag{4.1}$$

An inlier pixel must satisfy this condition for both the mean image and the variance image. If in either of these images it is denoted as outlier, the pixel is said to be *erroneous*. In case of the detection of too few or too many erroneous pixels, the multiply of the criterion should be adjusted. In the case of computed statistics, any exceptional outliers should be removed in order to not offset the standard deviation out of a reasonable range.

The outlier pixels represent an invalid measurement of the actual value, therefore they should be discarded from the following computation of Gaussian function.

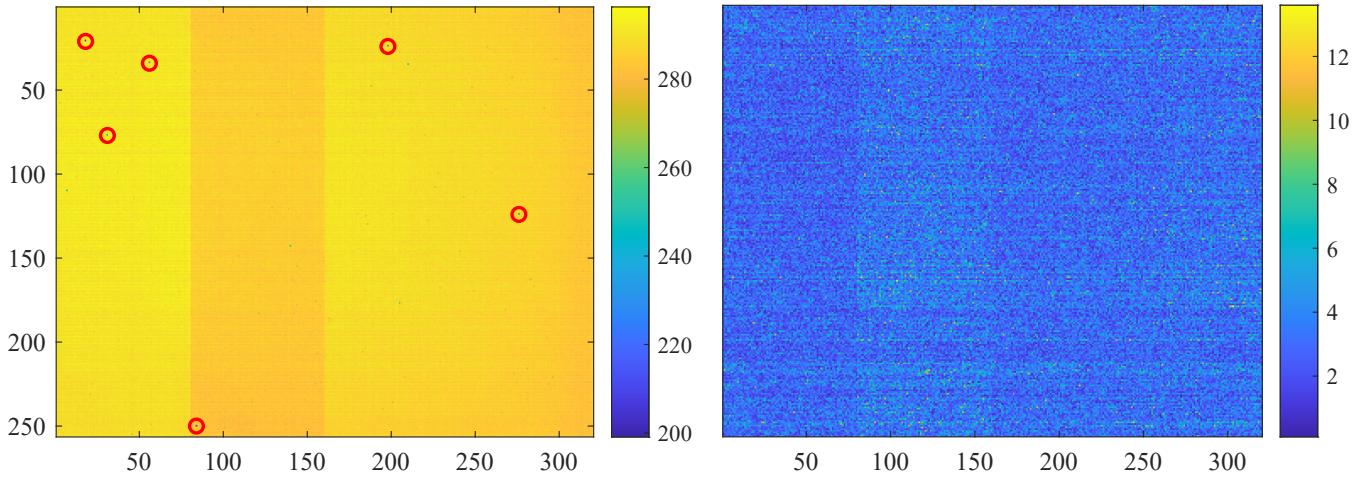

a) Mean b) Variance

Figure 4.3. Pixel's statistics for shutter speed 4.6 ms, lens cap off, taken by camera one. In mean image, outliers are marked as red circles. The inliers correspond to the interval $\langle 241.01,\ 333.52 \rangle$. No outliers were found in the computed variance image.

4.3 Features and pixel defects in camera one

This experiment aims to study the impact of shutter speed on dark images with uniform backgrounds. Ten dark images were captured by camera one at a shutter speed of 500 ms, which is the longest shutter speed that can be theoretically used for this type of application (the recommended value for applications would be 100-200 ms). The second collection of eleven images was shot at a shutter speed of 4.6 ms, the shortest exposure time available at the camera. This timing is often used for imaging a laser beam. Therefore, the shorter exposure times are more critical for the proper function of the measuring device.

A mean image for shutter speed 4.6 ms is shown in Fig. 4.3, where a darker vertical line is apparent. This camera has four analog-digital converters as well as camera two. These converters are each responsible for 80 columns, and therefore the band is caused by a different offset of converter number two. Nevertheless, as shown in Fig. 4.5, the most significant difference in values corresponds to a difference of ten intensity levels, which is only a 0.61‰ of camera's dynamic range. Next, the outliers in the pixel's mean intensities were detected, see Fig. 4.3 b). Pixels' variance was studied, results of which are shown in Fig. 4.3 b). As one may notice, the maximum variance goes up to 12, which corresponds to the value of 3.46 of standard deviation intensity levels, which comes to a 0.21‰ of camera's dynamic range. No significant outliers are identified in the variance image.

A set of ten dark images for a shutter speed of 500 ms were evaluated in the same manner. Mean image and variance image are shown in Fig. 4.4. The criterion of 15 standard deviations vouched for fifteen outliers in the mean image. All of the erroneous pixels identified at shorter exposure times are detected as well. Analysis of pixels' values variance has pointed out other three erroneous pixels.

Fig. 4.6 as well as Fig. 4.5 shows two cuts of mean dark image, averaged over ten pixel columns/rows. Notably, some intensity decline is apparent at the image corners. However, it is statistically insignificant in comparison to the intensity values of the center region.

A total of 18 erroneous pixels identified in camera one. From the results, it has been concurred that most pixel failures are detectable at longer shutters, which are not

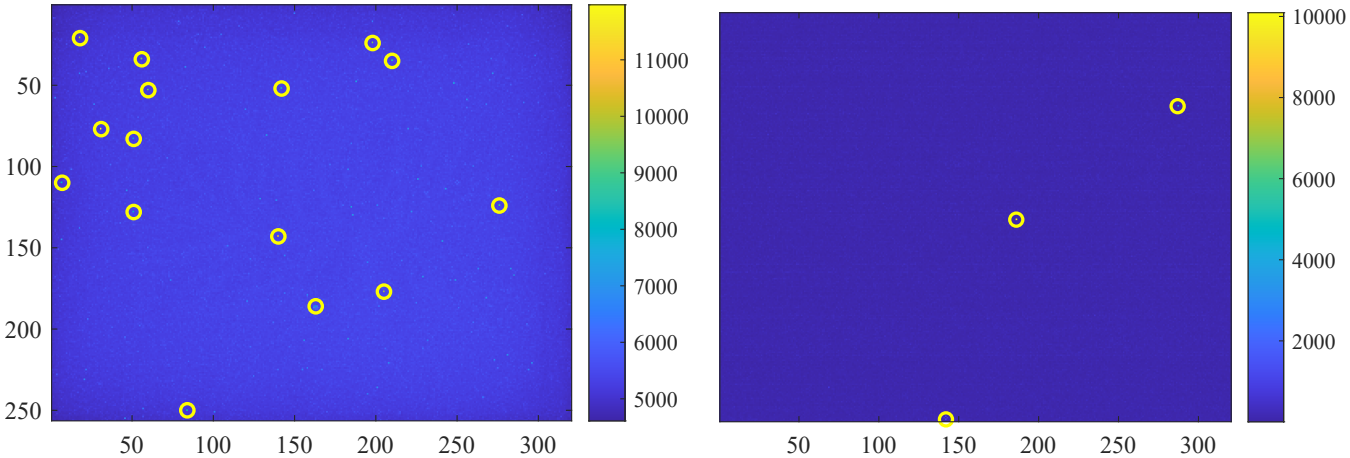

a) Mean b) Variance

Figure 4.4. Mean image and variance image for shutter speed 500 ms, lens cap off, taken by camera one. Outliers are marked as yellow circles, by the criterion described in equation (4.1), are outside of interval $\langle 2878.25, 7683.59 \rangle$ for the mean image and $\langle -857.18,\ 1075.90 \rangle$ for variance image.

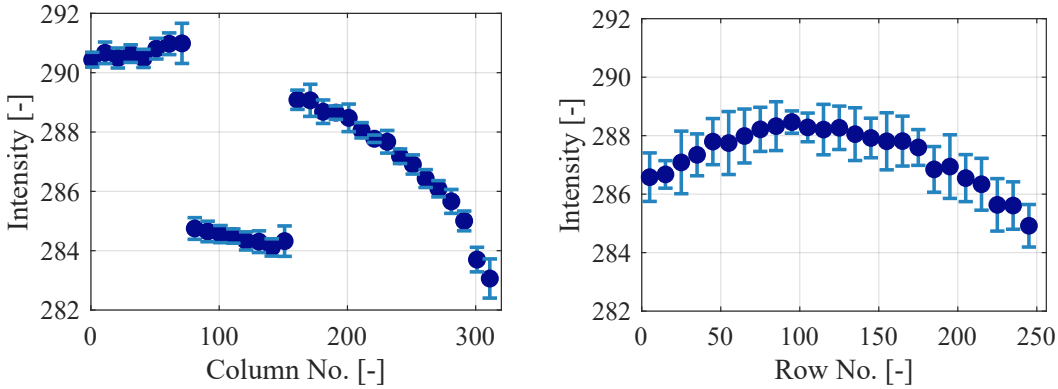

Figure 4.5. Mean pixel irradiance for 4.6 ms shutter speed for camera one. The blue dots represent averages of every 10 columns/rows with error bars equal to standard deviations.

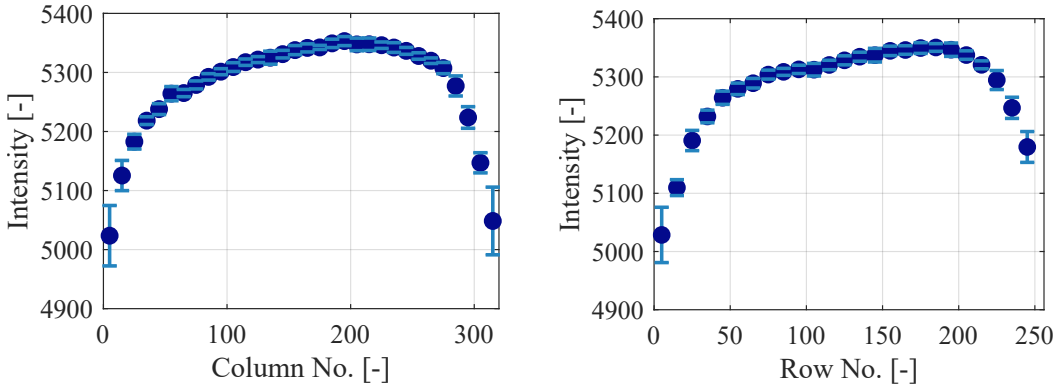

Figure 4.6. Mean pixel irradiance for 500 ms shutter speed for camera one. The blue dots represent averages of every 10 columns/rows with error bars equal to standard deviations.

intended to be used for imaging the region near the focal point. At shorter shutter speed the center of the image is clear of erroneous pixels, therefore the overall detection of the focal point and inclination angle should be affected minimally. A list of the erroneous pixels is in the Appendix A in Tab. A.1.

4.3.1 Intensity of dark image in camera one

Datasets of laser beam images captured by camera can be divided into two sub-categories by the used ND filters' optical density[1]. Their specific values are not known. For the sake of communication, they were referred to as *filter one, filter two, filter three,* as per their increasing intensity damp factor. ND filers were always used in a set of two, either filter one and filter three, or filter two and filter three. Therefore captured datasets reflect the imaging shutter speeds for each set of filters.

The combination of filter one and filter three lets through comparably more light than the combination of filter two and filter three. Therefore shorter shutter speeds ere used for capturing images with the combination of filters one and three.

Nine images were captured with filters one and three at different shutter speeds (4.6 ms, 7.5 ms, 10 ms, 20 ms, 30 ms, 50 ms, 75 ms, and 100 ms). For the filter combination of two and three images were captured at shutter speeds 75 ms, 100 ms, 120 ms, 150 ms, and 200 ms. Each image was statistically processed. The results are visualized in two *boxplots*, one for each sequence.

[1] Optical density of a material is a logarithmic intensity ratio of the light falling upon the material to the light transmitted through the material. Density= $-\log_{10}(I_0/I_1)$, where I_0 and I_1 are the intensities of incident and transmitted lights, respectively. [36]

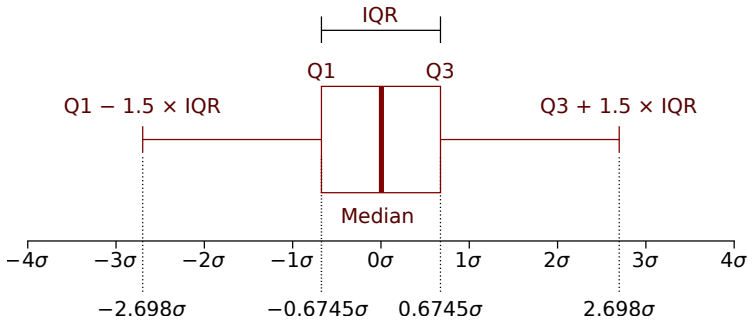

Figure 4.7. An example of a boxplot and its correlation to the σ values of normal distribuion. IQR $= Q_3 - Q_1$ denotes the inter-quartile range. The *whiskers* denote the interval $\langle Q_1 - 1.5\ \text{IQR},\ Q_3 + 1.5\ \text{IQR}\rangle$. Assimilated from [37].

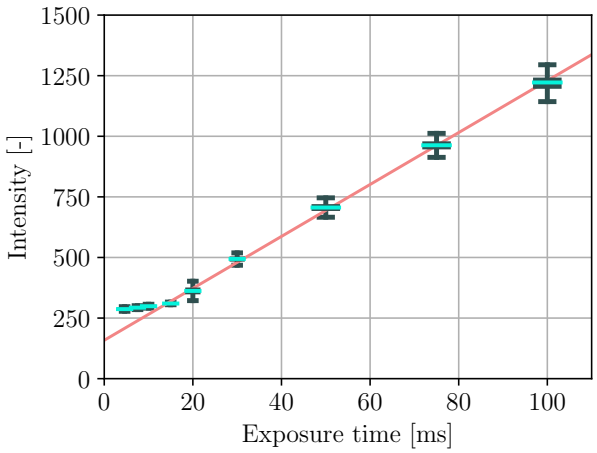

a) Filter one and filter three, $y = 10.71x + 158.40$

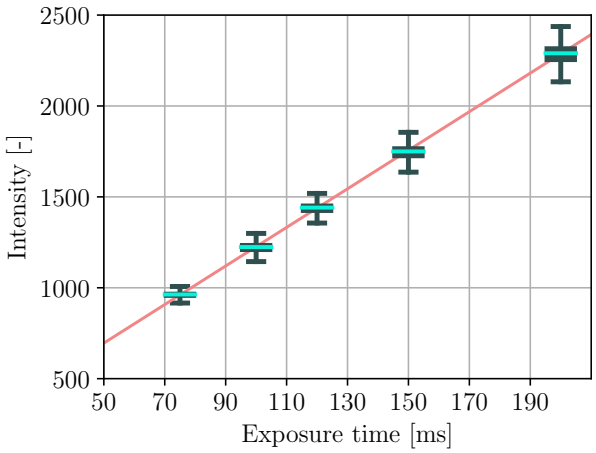

b) Filter two and filter three, $y = 10.61x + 165.08$

Figure 4.8. Dependence relation between the median intensities of dark images and shutter speed for camera one. The coral line is fitted to the medians (green) of exposure times longer than 15 ms.

The boxplot is a method for graphically demonstrating the spread of numerical data through their quartiles, see Fig. 4.7. The median value is noted as a bold line. The Q_i denotes the i-th quartile. The IQR $= Q_3 - Q_1$ is the so-called *inter-quartile range*, visualized as a box. The so-caleld *whiskers* denote the boundaries of the interval $\langle Q_1 - 1.5\ \text{IQR},\ Q_3 + 1.5\ \text{IQR}\rangle$.

The medians of each image at different shutter speeds were fitted by a line, as seen in Fig. 4.8. Camera exhibits non-linear dependency for exposure time lesser than 15 ms. Due to the fact that such short exposure times were not used for a combination of filter two and filter three, camera gain for datasets captured by them has linear camera gain dependency on shutter speeds.

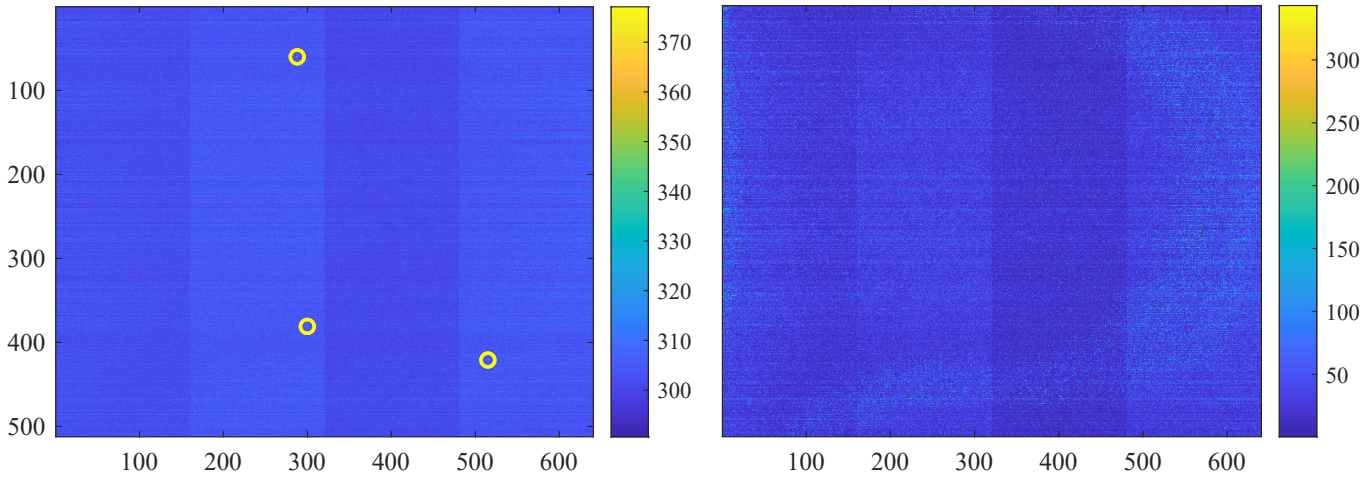

Figure 4.9. Pixel's statistics for shutter speed 16.7 ms, without the pixel [443, 484], lens cap off, taken by camera two. Outliers are marked as yellow circles. Inliers belong to the interval $\langle 265.85, 340.28 \rangle$ for the pixels' mean. No outliers in pixel's variance were found.

4.4 Features and pixel defects in camera two

All the images in the case of camera two were captured with camera lens zoom 20x and near-infrared absorptive ND filter with an optical density of 5.

An impact of a surrounding illumination on images with a uniform background was studied. For the purpose of detecting erroneous pixels, a set of images was acquired with different camera setups. A dataset was captured with the camera lens cap on and off. Furthermore, a difference invoked by different shutter speeds was examined. It can be reasonably argued that camera two will be operated at a shutter speed of 16.7 ms for laser beam imaging purposes. An initial position calibration, which induces searching for the laser's fitted lens, will demand a longer exposure time. For the user's comfort in adjusting camera position, a maximal exposure time of 200 ms is expected. However, the second used shutter speed was 500 ms. Combining these two explored parameter settings produced a dataset composed of four experiments (lens cap on — 4.6 ms, lens cap on — 500 ms, lens cap off — 4.6ms, lens cap off — 500 ms). Each set of images with fixed parameters was evaluated by calculating the mean of individual pixels values and computing corresponding variances.

The experiments have shown minimal differences in acquired images with the lens cap on and off. Pixel values differ by less than 0.5‰ for exposure times of 500 ms, and the differences are even substantially more minor for shorter shutter speeds. Hence, the datasets with lens cap off will be discussed below.

For the shutter speed of 16.7 ms, ten images with the lens cap off and ten images with the lens cap on were captured. Mean and variance images were. A mean intensity outlier was highlighted at position [443, 484]. Its mean value exceeds 3000, and it has a variance of approximately $1 \cdot 10^7$. Mean image without visualizing the pixel [443, 484] is shown in Fig. 4.9. Four distinct columns in the mean image are consistent with the four analog-digital converters used in the camera sensor.

Next, the variance of pixels was evaluated. The previously identified pixel [443, 484] is notable as well. On the grounds that its value overshadows the rest, it has been removed from visualization shown in Fig. 4.9. The difference between the row values in the mean and variance images of shutter speed 16.7 ms is statistically insignificant.

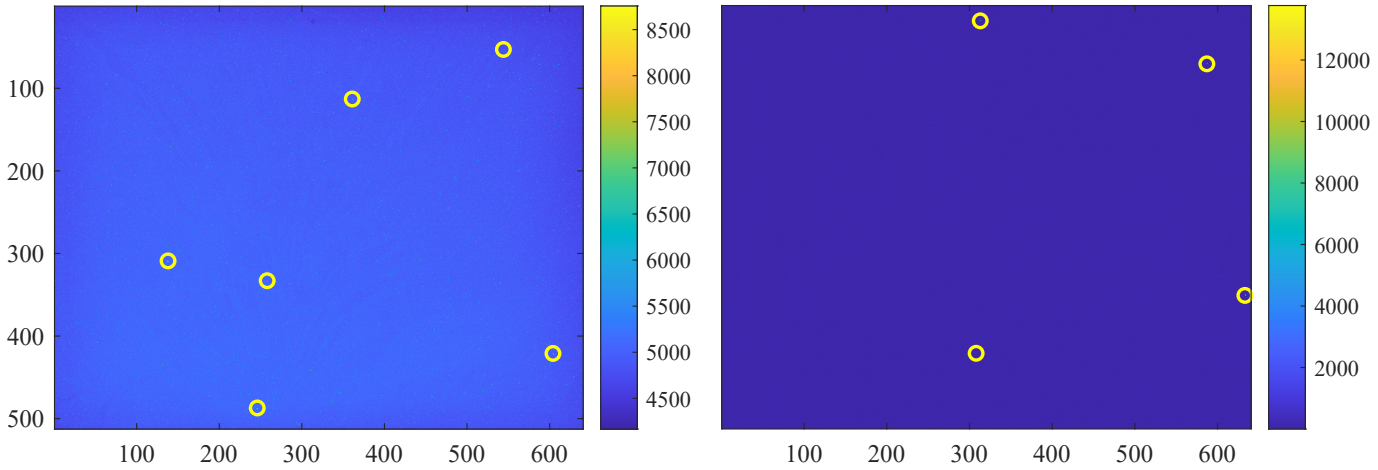

a) Mean b) Variance

Figure 4.10. Pixel's statistics for shutter speed 500 ms, without the pixel [443, 484], lens cap off, taken by camera two. Outliers are marked as yellow circles. Inliers belong to the interval $\langle 2890.92, 7050.05 \rangle$ for the mean image and $\langle -659.70, 839.91 \rangle$ for variance image.

As for the shutter speed of 500 ms, the same number of images under the same conditions were taken and processed equivalently. In Fig. 4.10 a), seven pixels (six pixels are shown plus an additional at position [443, 484]) in the pixel's mean image are determined as outliers. Due to the fact that these pixels were producing coherent outputs with the rest of the camera pixels at shorter exposure times, these are the cases of abnormally sensitive pixels. As for the variance image, four additional pixels are denoted as erroneous.

The Fig. 4.11 shows different intensity values of the pixel's at position [443, 484] captured in the camera two datasets with lens cap off and lens cap on for shutter speeds 16.7 ms and 500 ms. The pixels, as can be seen, produce semi-random values at four distinct layers for the shorter shutter speed. For the longer shutter speed values are at three distinct layers. This pixel is unable to provide relevant measurements, therefore its value should be discarded from the image processing.

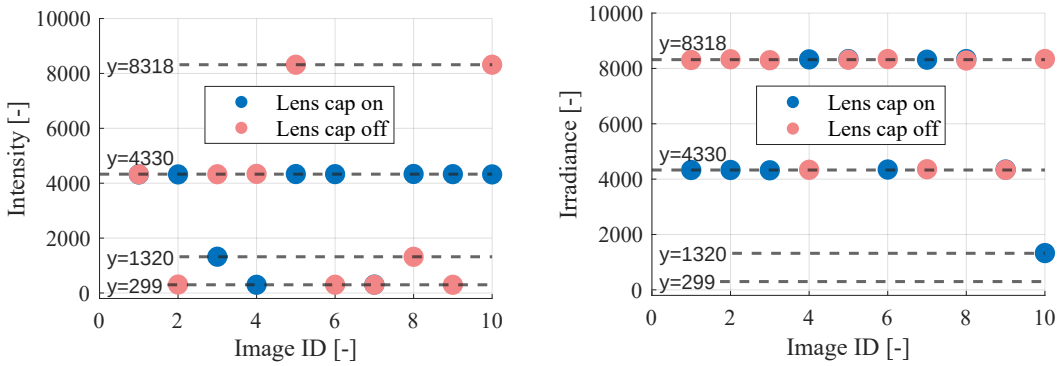

a) 16.7 ms b) 500 ms

Figure 4.11. Intensity values of the pixel [443, 484] in camera two for two shutter speeds with and without covered lens.

A total of 15 pixels were labeled erroneous in camera two. Three pixels showed an offset of approximately 23% of the mean value for shorter exposure times. Seven hypersensitive pixels were identified, with linear response to shutter speed, see Fig. 4.12.

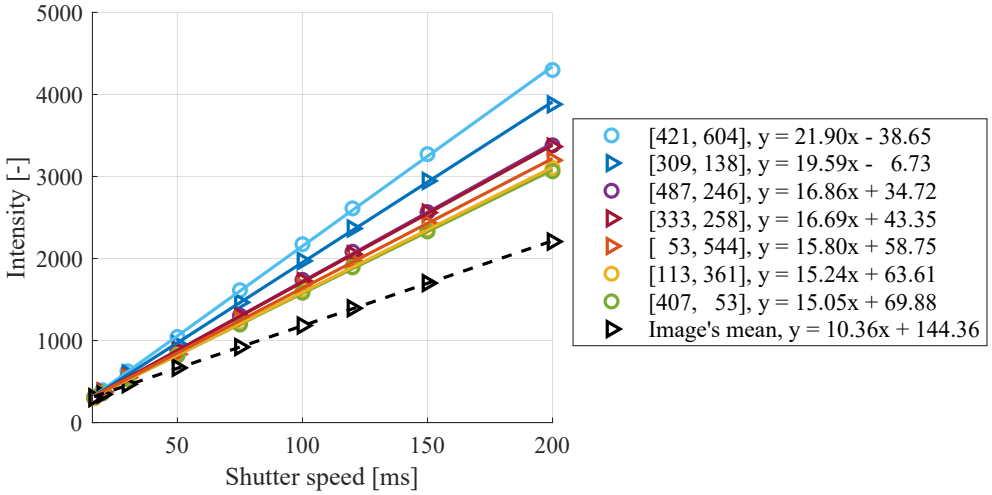

Figure 4.12. Intensity values of hypersensitive pixels in camera two and its dependency on shutter speed.

Then, other four problematic pixels with greater variance at longer exposure times were found. The most notable pixel [443, 484] exhibit a peculiar output pattern shown in Fig. 4.11. A list of identified erroneous pixels is in Appendix A in the Tab. A.2.

4.4.1 Intensity of dark image in camera two

An experiment evaluating dark image intensity at different shutter speeds was performed. Its task was to investigate if there is a linear dependency of these two parameters. A set of nine dark images with a uniform background was taken at different exposure times. The boxplots of the whole sequence are shown in Fig. 4.13. Unlike the case with the previous camera, described in section 4.3.1, the overall dependency of median image values on exposure times is linear. However, we can observe an offset of the 142.90 that is the most likely present due to the specific A/D converter parameters.

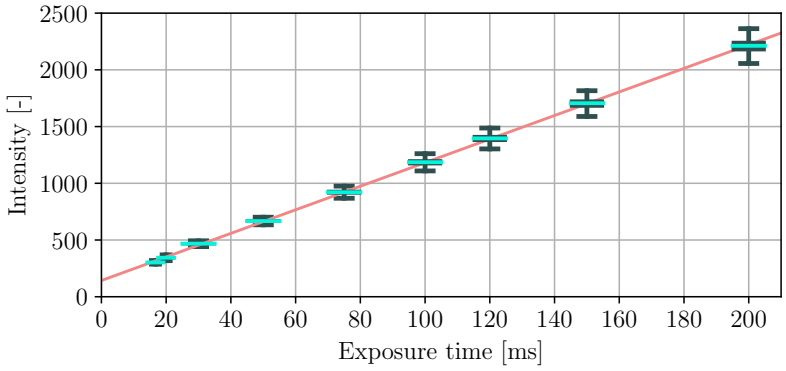

Figure 4.13. Dependence relation between the median intensities of dark images and shutter speed for camera two. The coral line $y = 10.39x + 142.90$ is fitted to the medians (green).

Chapter 5
Experiments

This chapter evaluates the overall performance of the designed algorithms. On top of that, it assesses algorithms' speed and robustness to image noise. Various experiments were conducted as the means of assessing the behavior of proposed algorithms under different circumstances. A chosen set of the performed experiments is described below.

5.1 Compared algoritms

Within the scope of this work, three algorithms for estimating the Gaussian beam's parameters were proposed. Two of which are of an iterative kind, based on non-linear least squares (LSQ) fitting. The last one is based on the estimation of covariance matrix directly from the dataset, according to equation (3.6). The algorithms will be regarded to as

- **Statistical** - non-iterative statistical Gaussian fit as described on page 24.
- **Direct** - iterative Gaussian fit with parameters θ, σ_x, σ_y as described on page 25.
- **ABC** - iterative Gaussian fit with parameters a, b, c as described on page 25.

The iterative algorithms need to be provided with an initial parameter estimate (*initial guess*), from which the parameter optimization is carried on. Two methods of determining these parameters were introduced in section Initial guess on page 27. The first one is based on the extreme irradiance pixels in the image (regarded as *Max*). The second one extracts the initial guess from fitting ellipse to a thresholded image (noted as *Ellipse*).

In some experiments a set of erroneous pixels is present. Their detection is described in Chapter 4, and lists of erroneous pixels for each camera are presented in Appendix A. The method chosen for mitigating the influence of the erroneous pixels on the algorithms was averaging. The pixel's value was replaced by the average in its 3×3 neighborhood. Its value was not considered during the averaging. This approach was possible due to the location of the laser beam in captured image. In the region near to the focal point the cross-section of the laser beam was located sufficiently far away from the erroneous pixels.

5.2 Datasets

Numerous datasets were captured of different micro-modules. The algorithms proposed in this work will be presented to the reader on three chosen datasets of real micro-modules.

- **Dataset A** consists of three independent measurements of the same micro-module. An operator provided reference of focal point position at 1.49 mm. The individual measurements are taken at shutter speeds 50 ms, 60 ms, and 75 ms. The supply current for the laser diode is unknown. Dataset was captured by camera one.

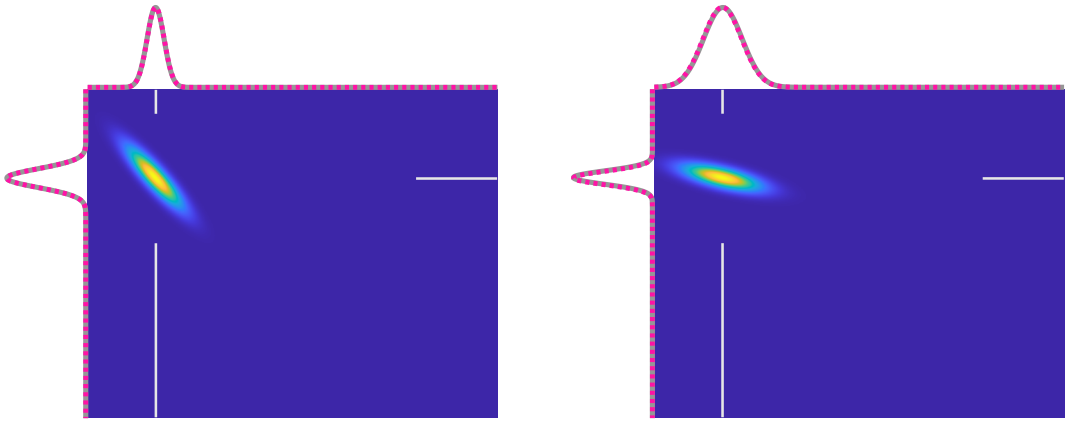

a) Direct - Ellipse b) Direct - Ellipse

Figure 5.1. Fitted Gauusian curves to D1 dataset. Gray lines represents axial image cuts, the pink dotted line is the cut of fitted 2D Gaussian. White lines point towards the center of the fitted Gaussian.

- **Dataset B** captured by camera one is of a micro-module with a specified focal point position by an operator at 1.38 mm. The laser beam was attenuated by the ND filter one and three and captured by the camera with lens magnification of 20 times. The supply current of the diode was 17 mA.
- **Dataset C** is captured by camera two. It is of a similar micro-module with an expected focal point of 1.5 mm. The reference for the focal point was not specified by an operator. The camera lens magnification was of 20 times. The diode supply current was 22 mA.

These datasets showcase a series of images of a real, manufactured micro-module without ground truth reference for focal point position. The camera setup is influenced by outside undetermined conditions, such as surrounding light, camera gain in relation to laser diode intensity, and dust particles on the camera matrix. Keeping that in mind, the actual reference parameters for the Gaussians curves are unknown.

For the testing purposes of the Gaussian function fitting, two synthetic datasets (D1, D2) were created artificially. The images of the Gaussian 2D function were generated in Matlab of size (512×640) px, re-casted as uint16 type, and saved in TIFF format, see Fig. 5.1.

- **D1 dataset** contains three generated images with known Gaussian parameters. The first two images were designed to determine the algorithm's ability to correctly estimate an ideal Gaussian function rotated by different angles, shown in Fig. 5.1. Furthermore, the third image introduced a simulation of an erroneous pixel close to Gaussian's center position. The pixel is located at position [78, 2] with a value of 14 200. The parameters of the image's generator equations are listed in Tab. 5.1 as ground truth.
- **D2 dataset** was designed to measure accuracy of processing a sequence of images, see Fig. 5.2. A set of twenty-one images was generated. It estimates z-cuts of an laser beam, as seen in our datasets, whose spot size cannot be accurately described by eq. (2.5). Instead, the beam waist changes in size more rapidly as the it approaches the focal point than when it distances from it. The focal point position of an artificial beam was set to 1.4 mm. Which was underlined by the simulated Gouy phase shift as well as the overall largest gain A. Its inclination angle is $\beta = 45°$ in xy plane and $\alpha = 8.13°$ in plane defined by z-axis and beam projection to xy-plane. The parameters Gaussian functions for all the images are in Appendix C.

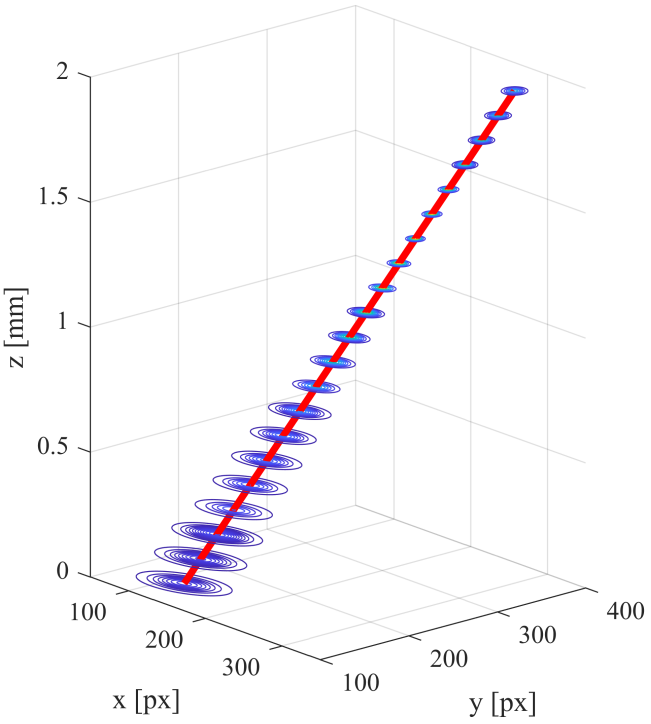

Figure 5.2. Propagation of the generated beam (red) in dataset D2. Every image from the dataset is represented as contour plot of the generated Gaussian function at given z position.

5.3 Resolution

A set of images of a calibration target were captured. The images were captured by camera one with the lens magnification of 20 times. Fig. 5.3 shows a resolution test target that is used for x, y axes calibration. The distances between each two bold lines were measured repeatedly. The results showed, that the distance of 100 μm correspond to 99 pixels, distance of 200 μm correspond to 198 pixels, and the distance of 300 μm correspond to 297 pixels. From which the pixel size was determined as 1 px = 1.01 μm. This conversion is used in the inclination angle computation, as well as for visualizing the results presented in this chapter.

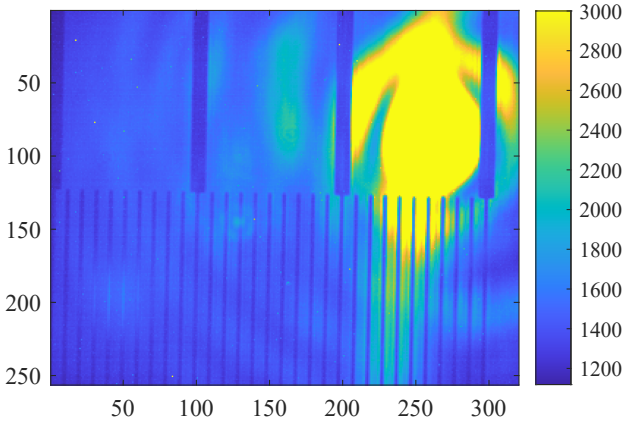

Figure 5.3. Resolution test target illuminated by a micro-module. The distance between bold stripes correspond to 100 μm. Image intensity is clipped at 3000 for visualization.

5.4 Goodness of Gaussian fit

Three algorithms for estimating the Gaussian beam parameters were tested on the generated dataset D1 that was described above, see Fig. 5.1. Table 5.1 compares reference values (ground truth) to the values that were fitted by the algorithms.

The Direct algorithm in combination with Max initial guess estimate produced partially incorrect results in the first image. The initial guess of the standard deviations (σ_z, σ_y) and the θ angle were significantly off in comparison to the ground truth. That caused the failure in the θ parameter, which in hindsight averaged the values of Gaussian's standard deviations. A 20-point increase in the offset I_0 is present. It equals the amount by which the gain A was reduced.

As for the results of the Statistical algorithm in the first image, the offset of the estimated Gaussian's standard deviation parameters is likely to be caused by the fact that the the Gaussian is located close to the image's edge. Part of the values relevant for fitting were cropped by the image frame. This should not pose a problem for the algorithm for most micro-modules, as they are imaged so that their projection in the region near the focal point is close to the image's center. The images taken further from the focal point are discarded by an IOA criterion in any case.

The second test image has proven to be rather tricky for the same two algorithms as the first image. The algorithms used in combination with the Ellipse initial guess estimation have successfully fitted both the first and the second test image.

The third test image with the erroneous pixel affected the Max method. Which cased the iterative algorithms to fail. Even though the algorithms with the initial guesses

	A [-]	x_0 [px]	y_0 [px]	σ_x [px]	σ_y [px]	θ [rad]	I_0 [-]
			Image one: $\theta = 0.837$ rad				
Ground truth	12 257.27	138.00	105.00	40.64	10.11	0.837	304.30
Direct - Max	9 827.26	138.00	105.00	21.08	19.25	1.510	324.11
Direct - Ellipse	12 257.26	138.00	105.00	40.64	10.11	0.837	304.02
ABC - Max	12 257.26	138.00	105.00	40.64	10.11	0.837	304.02
ABC - Ellipse	12 257.26	138.00	105.00	40.64	10.11	0.837	304.02
Statistical	12 252.67	138.00	105.00	35.80	9.97	0.839	304.00
			Image two: $\theta = 1.337$ rad				
Ground truth	12 257.27	138.00	105.00	40.64	10.11	1.337	304.30
Direct - Max	11 400.29	138.00	105.00	34.52	11.87	1.571	310.74
Direct - Ellipse	12 257.26	138.00	105.00	40.64	10.11	1.337	304.02
ABC - Max	12 257.29	138.00	105.00	40.64	10.11	1.337	304.01
ABC - Ellipse	12 257.29	138.00	105.00	40.64	10.11	1.337	304.01
Statistical	12 253.33	138.00	105.00	36.02	9.64	1.355	304.00
			Image three: Errorneous pixel				
Ground truth	12 257.27	138.00	105.00	40.64	10.11	1.337	304.30
Direct - Max			**Failed**				
Direct - Ellipse	11 400.29	138.00	105.00	40.64	10.11	1.571	310.78
ABC - Max			**Failed**				
ABC - Ellipse	12 257.28	138.00	105.00	40.64	10.11	1.337	304.06
Statistical	12 801.66	137.96	104.94	35.88	9.55	1.359	304.00

Table 5.1. Fitted Gaussian's parameters on three generated test-images from D1 dataset. Three Gaussian function fitting algorithms (Direct, ABC, Statistical) were tested with two methods for initial guess estimation (Max, Ellipse).

provided by the Ellipse method correctly identified the center coordinates (x_0, y_0) of the Gaussian and its standard deviation σ_x, σ_y, the Direct method under-fitted the gain A value and overestimated the θ angle.

Overall, the difference in gain A and offset I_0 as presented in the table 5.1 can be explained by the discretization of values performed in the image grid.

5.5 Correspondence to manual results

This section processes the images from the dataset A. This dataset contains three sequences captured at different shutter speeds (50 ms, 60 ms, and 75 ms). They were taken on the original measuring device, where the camera's linear positioning axis was manually adjusted. The operator estimated the focal point for the datasets at position 1.49 mm. Therefore, this experiment compares the results provided by different proposed algorithms to the manual results obtained by operators. The dataset captured at an exposure time of 75 ms contains overexposed images. This type of error poses significant difficulties for curve fitting algorithms.

All three algorithms (Direct, ABC, Statistical) were compared in this section. The iterative algorithms were tested with initial guesses provided by the Max method. The comparison of the results is shown in Fig. 5.4. The iterative methods indicate a focal point at a systematically different location than the non-iterative method. A possible explanation could be, that the behavior was caused by a so-called Gaussian focal shift, described on page 12. It refers to the phenomenon when the laser beam's waist location is offset from the maximal beam irradiance by a lens in the optical path.

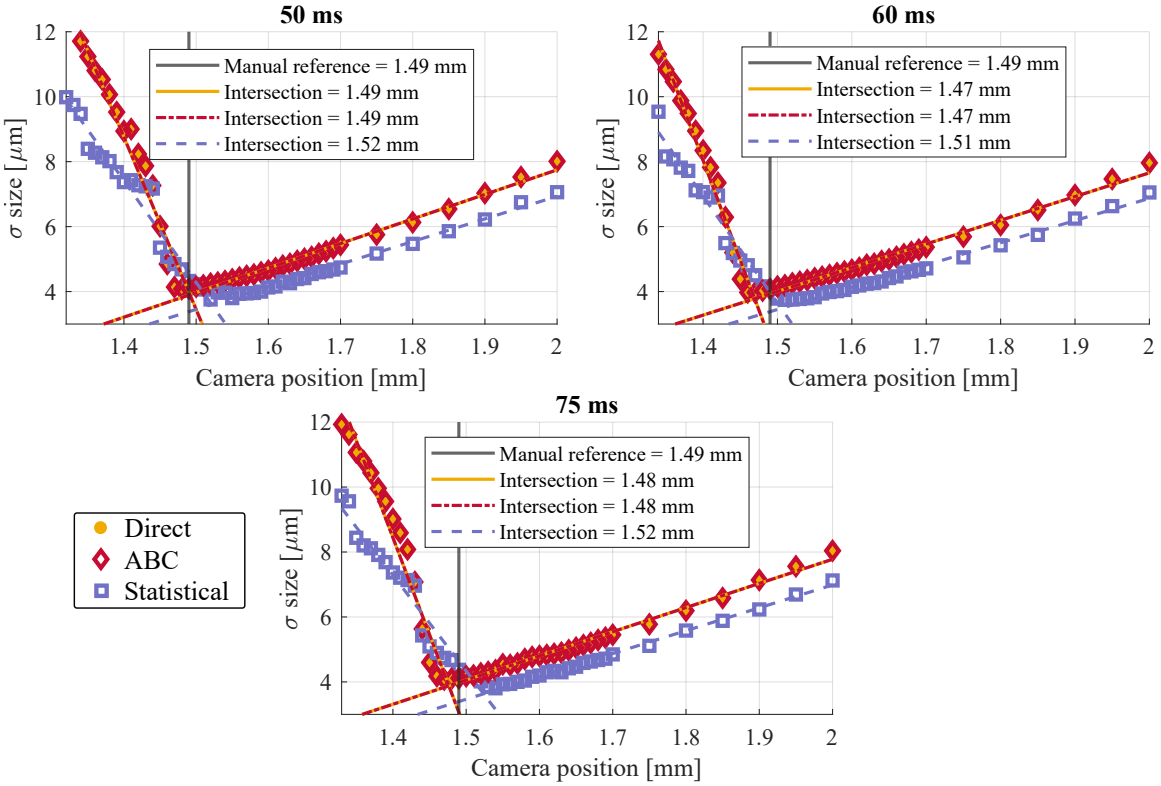

Figure 5.4. Comparison of focal point position estimates for sequences from dataset A of a single micro-module captured at different shutter speeds. The standart deviation of the intersections' abscissa is ±0.01 mm (rounded to two decimals) for all algorithms, computed by eq. (3.21).

This causes the non-iterative fitting algorithm to be biased towards later laser beam's propagation distances.

At a given sequence all of the algorithms provide stable results in the focal point and inclination angle for a given image. Some variance in results between two different datasets of a single micro-module may occur. It can be caused for example by a misalignment of the origin to the camera position or micro-module position shift caused by manipulation. On the pixel level, the difference may be caused by a different discretization of irradiance by pixels in the camera or by a presence of an erroneous pixel value, which was may not have occurred in the previous image capturing sessions.

The standard deviation of the intersection's abscissa, which corresponds to the focal point position, was determined to be ± 0.01 mm for all of the tested algorithms. As was previously mentioned, under normal circumstances, an operator should be able to detect the focal point position to a precision of tenths of a millimeter. Even though different operators may guesstimate the positions at different locations. Due to these facts, the algorithms provide a reasonably good estimates of focal point.

5.6 Effects of initial guess on real datasets

As mentioned in section 3.3, iterative algorithms' performance strongly depends on the precision of the initial guess. In cases where the initial guess did not adequately describe the captured laser beam, the fitting algorithm often failed to find any reasonable solution. Erroneous pixels may cause problems for these estimation methods. One way of mitigating such problems is to locate the erroneous pixels and remove their values. The method for dealing with erroneous pixels was described in section 5.1.

The dataset C used in this experiment is captured by camera two. Table 5.2 compares two methods of the initial guess estimation for the non-linear LSQ fit (for both the Direct and the ABC algorithms). Namely, table evaluates the number of performed iterations on per image basis, as well as the sum of residuals normalized by number of pixels in the intensity image. The mean value of residuals for both the Direct algorithm and the ABC algorithm is reasonably close. The initial parameter estimation by an Ellipse method performs better for both algorithms. Overall the ABC algorithm converges faster than the Direct algorithm.

		Direct		ABC	
		Max	Ellipse	Max	Ellipse
No. of Iterations	Mean	16.2	12.5	13.1	12.5
	Q_1	12.0	10.0	10.0	10.0
	Q_2	16.0	11.0	13.0	12.0
	Q_3	19.0	14.0	15.5	14.0
$\bar{r}_i$	Mean	82.49	64.92	83.54	64.97
	Q_1	20.69	19.24	20.78	19.51
	Q_2	42.50	38.87	41.70	38.87
	Q_3	92.21	65.98	92.21	65.98

Table 5.2. Impact of different methods of initial guess estimation on number of iterations and final error per pixel. Q_i represents i-th quartile.

		Direct		ABC	
		Max	Ellipse	Max	Ellipse
No. of Iterations	Mean	14.7	12.4	12.3	12.5
	Q_1	10.0	9.0	8.0	9.0
	Q_2	15.0	11.0	12.0	11.0
	Q_3	17.0	14.0	14.0	14.0
$\bar{r}_i$	Mean	35.82	35.62	37.78	35.75
	Q_1	30.73	34.28	34.28	34.28
	Q_2	14.11	14.56	15.43	15.41
	Q_3	40.28	42.57	44.99	42.57

Table 5.3. Impact of different methods of initial guess estimation on number of iterations and final error per pixel. Only the results of the fits that satisfy the IOA$>$ 30%IOA$_{\max}$ condition are shown. Q_i represents i-th quartile.

Table 5.3 compares statistics of the successful fits that satisfy the threshold of IOA$>$ 30% of maximal IOA value in the dataset are processed. The Parametric—Max algorithm failed to fit 8 curves, and 27 more fits did not satisfy the IOA condition. The Parametric—Ellipse method successfully fitted all the images in the dataset. The IOA criterion discarted 29 fits in total. The ABC—Max failed to fit two curves and discarded 29 fits. The ABC—Ellipse combination successfully fitted all the images and discarded the same 29 fits by the IOA criterion. Overall, the results presented in this table are more preferable than in the table 5.2.

A comparison to the Statistical method was made. Erroneous pixel values in images were replaced by mean value of their neighborhood, during the image preprocessing phase. The difference in the results for the iterative algorithms with and without preprocessed erroneous pixels is statistically minimal. For results on images with masked pixels see Appendix C Tab. C.4 .

The Tab. 5.4 shows results produced by the Statistical algorithm, where the Raw rows represent images with the non-preprocessed pixels, and the Preprocessed rows correspond to the images with fixed erroneous pixels (as was described in section 5.1). The minimal difference in the results may be explained by the fact that the erroneous pixels were located far enough from the laser beam in the image and did not cause much disturbance in the fit.

		Mean	Q_1	Q_2	Q_3
Raw	All	70.27	19.49	32.12	126.71
	Successful	62.30	18.75	23.71	93.46
Preprocessed	All	70.51	19.74	32.10	126.71
	Successful	62.29	18.74	23.70	93.46

Table 5.4. Residuals per pixel of the *Statistical* fit with fixed erroneous pixels. Q_i represents i-th quartile. Unlike in Raw images, the erroneous pixel values are removed in Preprocessed images.

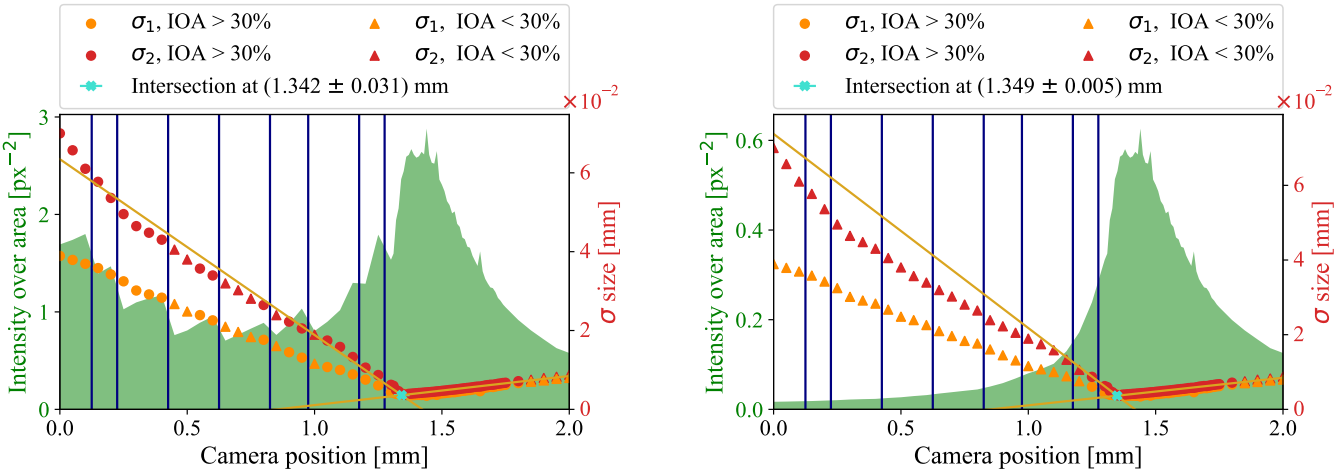

a) Non-normalized shutter

b) Normalized shutter

Figure 5.5. Effects of shutter speed normalization on IOA in dataset B captured by camera one. Values normalized by $y = 10.71$ shutter speed $+ 158.40$ (see section 4.3.1). In images the visualized σ_i are in relation $\sigma_1 < \sigma_2$. Vertical lines denote shutter speed change.

5.7 Effects of shutter speed change on real datasets

The images in dataset B were captured at different shutter speeds (100 ms, 75 ms, 50 ms, 30 ms, 20 ms, 15 ms, 10 ms, 7.5 ms, and 4.6 ms). Fig. 5.5 shows a comparison of processing the adjusted and the non-adjusted individual images for the camera's intensity of the dark image (described in Chapter 4). In IOA is normalized as is described in section 3.6. Even after normalization, the IOA curve is not smooth for these results. An incorrect timing for shorter exposure times may have caused a problem in the dataset B or some other unknown external effects on the micro-module. The laser beam's gain A grows in some cases instead of decreasing its value after passing the focal point. This may also clarify the difference in results provided by the algorithms (1.34 mm, 1.35 mm) and the operator's assigned focal position (1.38 mm).

In contrast, the phenomenon does not appear in the dataset C in Fig. 5.6. These images were taken with exposure times of 300 ms, 200 ms, 150 ms, 120 ms, 75 ms, 50 ms, 30 ms, 20 ms, and 16.7 ms.

Even though the effect of non-normalized images for the shutter speeds may be minimal for the focal point estimation, further experiments show that it becomes more pronounced for estimation of the inclination angle.

5.8 Inclination angle estimation

This section investigates the accuracy of inclination angle estimation, as well as the effects of the image normalization by shutter speed. The accuracy is tested on the artificial dataset D2. And then the effects of image normalization for IOA calculation are highlighted on the dataset C. The results were computed using the ABC algorithm with initial estimation created by the Ellipse method.

Fig. 5.7 shows results on the dataset D2, the algorithm correctly estimated the focal point at position 1.40 mm. Next, the inclination angle in both of the perpendicular planes were computed correctly. The reference values are $\alpha = 8.13°$ and $\beta = 45°$.

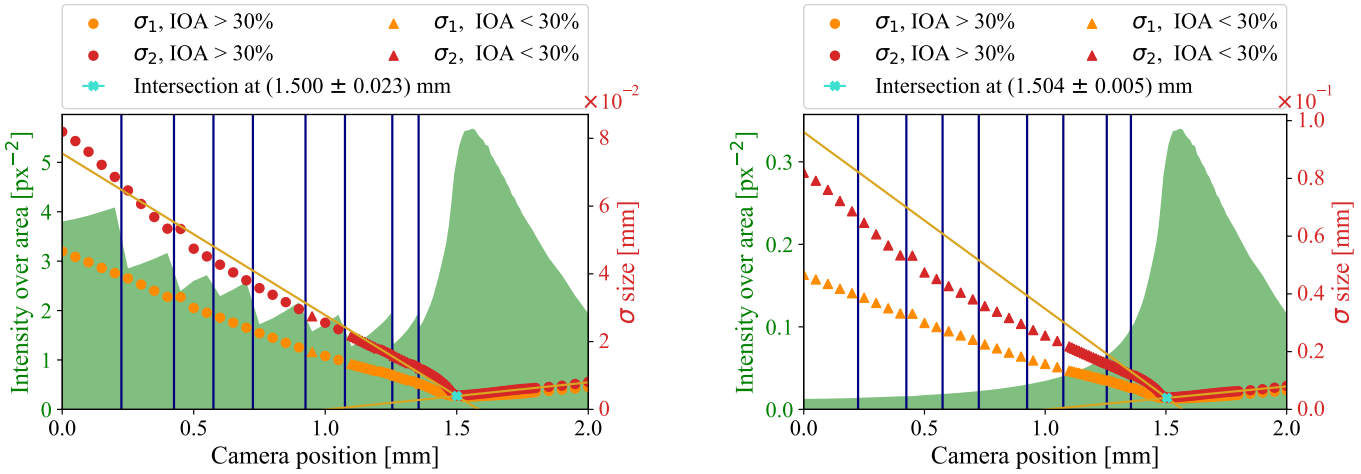

a) Non-normalized shutter

b) Normalized shutter

Figure 5.6. Effects of shutter speed normalization on IOA in dataset C captured by camera two. Values normalized by $y = 10.39 \text{ shutter} + 142.90$ (see section 4.4.1). In images the visualized σ_i are in relation $\sigma_1 < \sigma_2$. Vertical lines denote shutter speed change.

Results can be seen in Fig. 5.8. The complete results are in Appendix C. The ABC algorithm performed well on both occasions.

For the dataset C, the manufacturer sets the α-angle of the micro-module to 2–3 degrees, which correspond to the results in Fig. 5.9. The laser's beam values for the β-angle are not specified.

In Fig. 5.10 an algorithm failed to compute the correct β-angle for non-normalized shutter data. The data points in Fig. 5.10 deviate from straight-line significantly as they advance from the focal point. In contrast to Fig. 5.9, the fitted data points were more likely to be in a semi-straight line as they travel in the direction of laser beam propagation. This is caused by the algorithm's failure to adjust for the discrepancies between an ideal Gaussian beam propagation and the real point spread function, which was described in section 2.3.

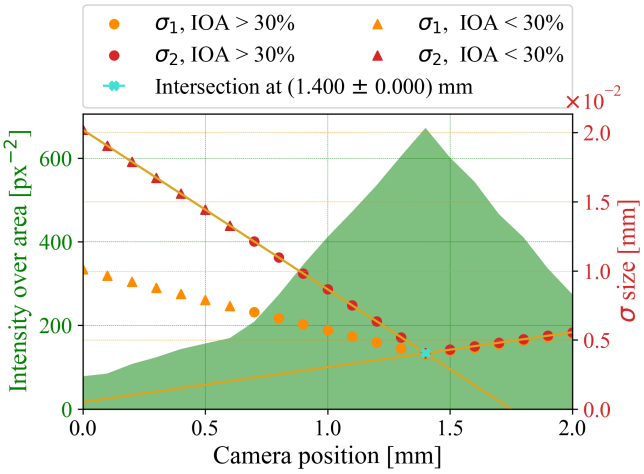

Figure 5.7. Computed results of the generated dataset D2. The visualized σ_i are in relation $\sigma_1 < \sigma_2$.

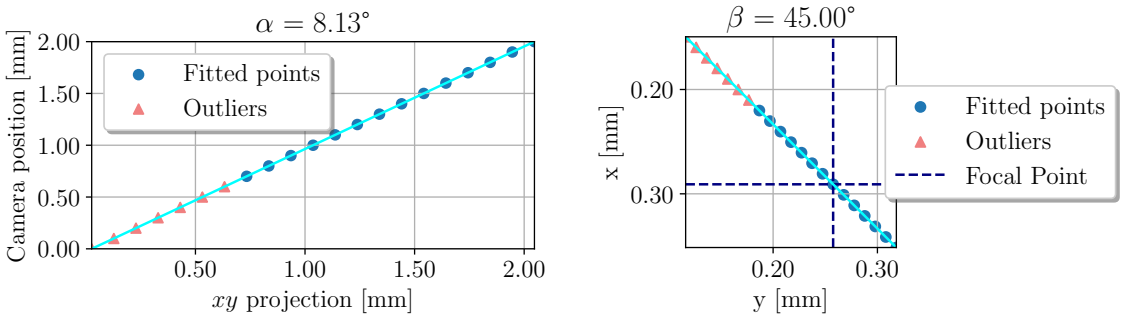

Figure 5.8. Computed inclination angle for generated dataset D2.

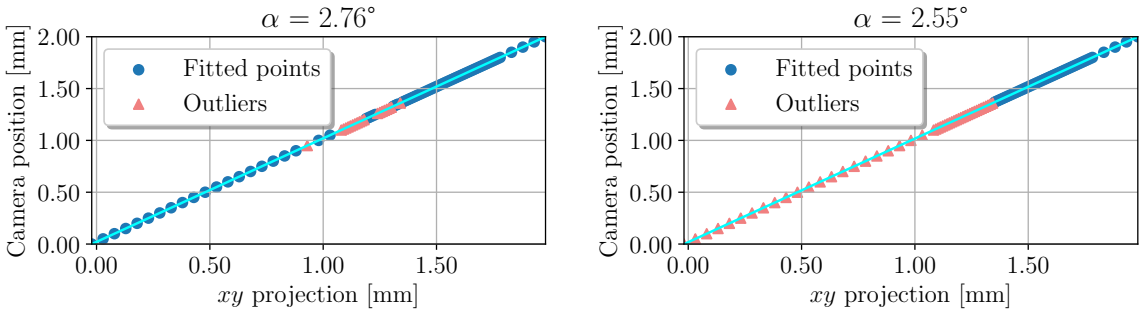

a) Non-normalized shutter b) Normalized shutter

Figure 5.9. Effects of shutter normalization on α angle estimation for dataset C.

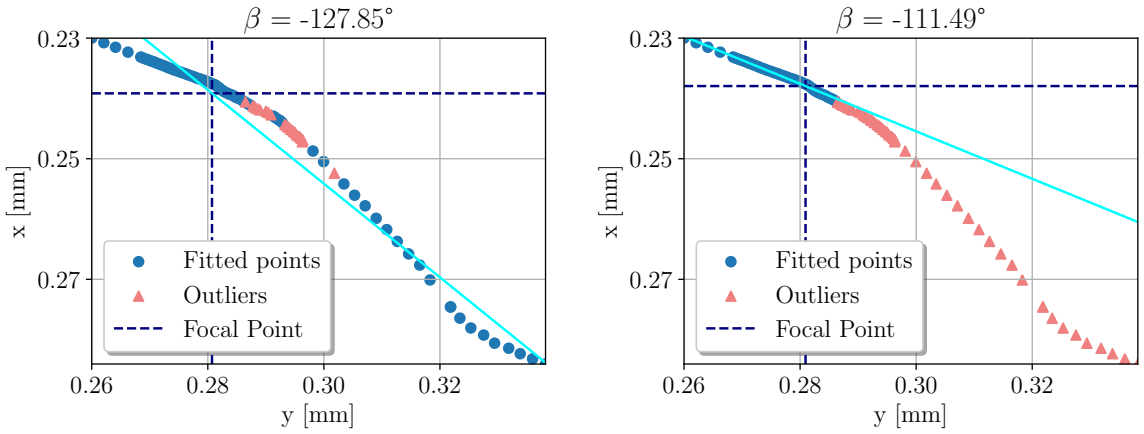

a) Non-normalized shutter b) Normalized shutter

Figure 5.10. Shutter normalization effects on β angle estimation for dataset C.

Chapter 6
Conclusion

This thesis focuses on estimating the parameters of a laser beam emitted by a micro-module. We studied the propagation and the geometry of a laser beam emitted by a semiconductor laser. Based on the gained insight, several algorithms were developed to estimate laser beam parameters: inclination angle and the focal point position. The input of the algorithms is a sequence of images captured at different propagation distances of the laser beam. The algorithm, designed to determine the laser beam's focal point position and inclination angle, evaluates the parameters extracted from the entire sequence of images. The algorithms that approximate laser beam cross-section by a two-dimensional Gaussian function operate at the level of a single image.

Three algorithms were proposed for the Gaussian function fitting. In the simplest case, the parameters of the Gaussian function were estimated by an analytically computed covariance matrix. This approach runs 55 times faster than other implemented algorithms. However, it can produce inaccurate results when an image frame crops the laser beam. The other two algorithms for Gaussian function fitting are based on non-linear least-squares estimation in a constrained region. The results provided by the algorithms are more precise and robust toward individual pixel intensity error than the non-iterative algorithm. The methods differ in the fitted parameter definition. The initial iterative approach was sub-optimal in some edge cases. Therefore, its modification was implemented, which provided more accurate results and faster convergence.

Both of the non-linear least-squares methods require an initial guess. Its determination is crucial for the algorithm's convergence. The first method for initial guess estimation is based on detecting the brightest and the darkest pixel. It may cause the iterative algorithms to fail in images with pixels that wrongly detect higher intensities. Therefore a second method for estimating the initial guess was introduced. It fits an ellipse on a thresholded image. The initial guess is then based on the ellipse's parameters.

After successfully fitting the Gaussian function, an algorithm processes a sequence of its standard deviations to determine the focal point position. We suppose that the focal point coincides with the laser beam waist. The algorithm fits two lines to the larger standard deviation in each image. The intersection of the two lines corresponds to the focal point position. In the next step, the inclination angle is estimated. The Gaussians' center positions alongside the propagation axis are approximated by a line, from which the inclination angle is computed.

Performed experiments shown in this work prove that the algorithms are stable and provide relevant results. The estimate of the focal point position is determined with an accuracy of 0.01 mm in the presented datasets. The estimated inclination angle adheres to the known references. The algorithms comply with the provided specifications in their intended use case.

References

[1] Hecht, J. *Understanding lasers*. 4. ed. Piscataway, NJ: IEEE Press, 2019. ISBN 978-1-119-31064-8.

[2] Hecht, E. *Optics*. England, UK: Pearson Education, Incorporated, 2017. ISBN 978-1-292-09693-3.

[3] Svetlo, O. *Principles of Lasers*. 5. ed. New York: Springer, 2010. ISBN 978-1-4419-1301-2.

[4]

[5] Gross, H. *Handbook of Optical Systems*. 1. ed. Weinheim: Wiley-vch, 2005. ISBN 35-274-0378-5.

[6] Chang, W. S. C. *Principles of lasers and optics*. Cambridge: Cambridge University Press, 2007. ISBN 05-216-4535-2.

[7] Kochkina, E. *Stigmatic and Astigmatic Gaussian Beams in Fundamental Mode*.

[8] Paschotta, R. *Gaussian Beams*. [cit. 2022-03-28]. `https://www.rp-photonics.com/gaussian_beams.html`.

[9] *Lasers and laser-related equipment - Test methods for laser beam widths, divergence angles and beam propagation ratios*.

[10] Paschotta, R. *Gouy Phase Shift*. [cit. 2022-03-28]. `https://www.rp-photonics.com/gouy_phase_shift.html`.

[11] *Laser Optics Resource Guide*. [cit. 2022-03-25]. `https://www.edmundoptics.com/knowledge-center/application-notes/lasers/laser-optics-resource-guide/`.

[12] Cai, Y., and Q. Lin. The elliptical Hermite-Gaussian beam and its propagation through paraxial systems. *Optics Communications*. 2002, Vol. 207, No. 1, pp. 139-147. Available from DOI https://doi.org/10.1016/S0030-4018(02)01533-X.

[13] Mei, Zh., J. Gu, and D. Zhao. The elliptical Laguerre-Gaussian beam and its propagation. *Optik*. 2007, Vol. 118, No. 1, pp. 9-12. Available from DOI 10.1016/j.ijleo.2005.12.012.

[14] Nasse, M. J., and J. C. Woehl. Realistic modeling of the illumination point spread function in confocal scanning optical microscopy. *J. Opt. Soc. Am. A*. OSA, Feb, 2010, Vol. 27, No. 2, pp. 295–302. Available from DOI 10.1364/JOSAA.27.000295.

[15] Sakurambo. *Airy-pattern.svg*. `https://commons.wikimedia.org/wiki/File:Airy-pattern.svg`.

[16] Paschotta, R. *Optical Aberrations*. [cit. 2022-03-28]. `https://www.rp-photonics.com/optical_aberrations.html`.

[17] Schmidt, J. D. *Numerical simulation of optical wave propagation with examples in MATLAB*. 1. ed. USA: SPIE, 2010. ISBN 978-0-8194-8326-3.

[18] Sheu, F.-W., and Ch.-H. Chang. Measurement of the intensity profile of a Gaussian laser beam near its focus using an optical fiber. *American Journal of Physics*. 2007, Vol. 75, No. 10, pp. 956-959. Available from DOI 10.1119/1.2723797.

[19] Hossain, Md A., J. Canning, K. Cook, and A. Jamalipour. Smartphone laser beam spatial profiler. *Opt. Lett.* OSA, Nov, 2015, Vol. 40, No. 22, pp. 5156–5159. Available from DOI 10.1364/OL.40.005156.

[20] Bonnett Del Alamo, M., C. Soncco, R. Helaconde, J. L. Bazo Alba, and A. M. Gago. Laser spot measurement using simple devices. *AIP Advances*. 2021, Vol. 11, No. 7, pp. 075016. Available from DOI 10.1063/5.0046287.

[21] Roundy, C. B., and K.D. Kirkham. Current technology of laser beam profile measurements. *Laser beam shaping*. Citeseer, 2014, pp. 463–524.

[22] Keaveney, J. Automated translating beam profiler for in situ laser beam spot-size and focal position measurements. *Review of Scientific Instruments*. 2018, Vol. 89, No. 3, pp. 035114. Available from DOI 10.1063/1.5022973.

[23] Guttenova, J. Laser beam scanning by mechanical devices and CCD camera. In: *14th Slovak-Czech-Polish Optical Conference on Wave and Quantum Aspects of Contemporary Optics*. SPIE, 2006. pp. 342 – 349. Available from DOI 10.1117/12.638977.

[24] Alexeev, I., J. Wu, M. Karg, Z. Zalevsky, and M. Schmidt. Determination of laser beam focus position based on secondary speckles pattern analysis. *Appl. Opt.* OSA, Sep, 2017, Vol. 56, No. 26, pp. 7413–7418. Available from DOI 10.1364/AO.56.007413.

[25] Wasserman, L. *Random Variables*. New York, NY: Springer New York, 2004. ISBN 978-0-387-21736-9.

[26] Jolliffe, I.T. *Principal component analysis*. 2nd ed ed. New York: Springer, 2002. ISBN 03-879-5442-2.

[27] Price, G. R. Extension of covariance selection mathematics. *Annals of Human Genetics*. 1972, Vol. 35, No. 4, pp. 485-490. Available from DOI 10.1111/j.1469-1809.1957.tb01874.x.

[28] *Scipy.optimize.least_squares*. [cit. 2022-04-06]. https://docs.scipy.org/doc/scipy/reference/index.html.

[29] Martin, J., G.D. Martin, and A.G. Asuero. Intersecting Straight Lines: Titrimetric Applications. In: 2017. ISBN 978-953-51-3523-4. Available from DOI 10.5772/intechopen.68827.

[30] Werner, T. *Optimalizace*. Praha, 2020.

[31] *InGaAs cameras*. [cit. 2022-02-13]. https://www.hamamatsu.com/eu/en/product/cameras/ingaas-cameras.html.

[32] *InGaAs area image sensor G13393-0909W*. [cit. 2022-02-13]. https://www.hamamatsu.com/content/dam/hamamatsu-photonics/sites/documents/99_SALES_LIBRARY/ssd/g13393-0909w_kmir1027e.pdf.

[33] *M Plan Apo NIR 20X , Item No. 378-824-5*. https://shop.mitutoyo.eu/.

[34] Optics, Edmund. *Optics and photonics catalog & resource guide — 2022*.

[35] Ghosh, S., D. Froebrich, and A. Freitas. Robust autonomous detection of the defective pixels in detectors using a probabilistic technique. *Appl. Opt.* 2008, No. 47, pp. 6904-6924. Available from DOI https://doi.org/10.1364/AO.47.006904.

[36] Zhang, J.X.J., and K. Hoshino. *Molecular Sensors and Nanodevices: Chapter 5 - Optical Transducers*. Oxford: William Andrew Publishing, 2014. ISBN 978-1-4557-7631-3. Available from DOI https://doi.org/10.1016/B978-1-4557-7631-3.00005-3.

[37] Jhguch. *Boxplot and a probability density function (pdf) of a Normal N(0,1σ^2) Population.* [cit. 2022-05-13]. https://commons.wikimedia.org/wiki/File:Boxplot_vs_PDF.svg.

Appendix A
Dark images processing

This appendix contains some of the results of the dark image processing used for determining the erroneous pixels in cameras, see section 4.2.

A.1 Camera one

The results of processing the images captured by camera one are presented below. The table A.1 states the mean and variance values for two shutter times of identified erroneous pixels. The figures A.1 and A.2 present histograms of computed mean image.

	4.6 ms		500 ms	
Position	Mean	Variance	Mean	Variance
[77, 31]	237.80	0.84	11 973.70	543.34
[143, 140]	252.10	1.43	10 451.10	192.77
[21, 18]	199.10	1.88	9 927.00	95.11
[177, 205]	260.70	5.79	9 887.70	119.79
[24, 198]	218.10	2.99	9 523.20	31.07
[34, 56]	233.60	2.71	9 434.10	173.21
[53, 60]	296.30	2.68	9 211.10	102.10
[124, 276]	240.80	1.51	8 876.70	136.46
[35, 210]	255.40	0.49	8 522.80	47.96
[52, 142]	290.20	3.73	8 302.40	212.93
[250, 84]	207.30	2.90	8 191.10	124.77
[128, 51]	294.90	4.54	8 187.50	164.06
[110, 7]	256.40	2.27	8 029.20	113.96
[186, 163]	279.20	4.40	8 015.00	111.11
[83, 51]	296.30	4.68	8 000.10	160.77
[130, 186]	273.40	1.38	7 179.70	10 092.50
[59, 287]	286.40	2.71	5 395.50	4 266.06
[255, 142]	281.40	6.04	5 215.60	1 136.00

Table A.1. Identified errorneous pixels (camera one).

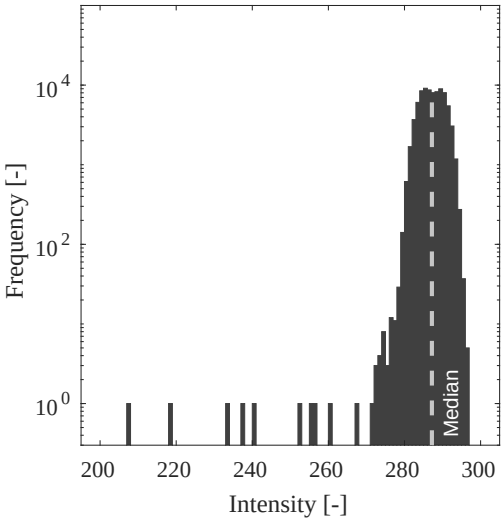

Figure A.1. Histogram of mean image (Fig. 4.3) with shutter speed 4.6 ms.

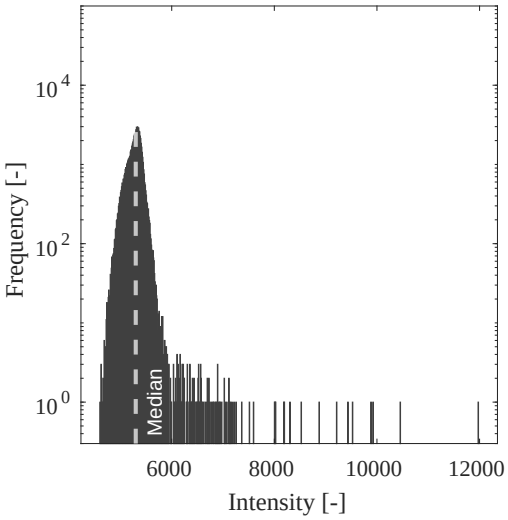

Figure A.2. Histogram of mean image (Fig. 4.4) with shutter speed 500 ms.

A.2 Camera two

Results of dark images processing, that were captured for determining erroneous pixels in camera two. Four datasets were created in total. Two datasets were captured at 4.6 ms exposure time and the other two at 500 ms. The difference in the datasets of the same shutter speed is that one was captured with a lens cap on and the other had a lens cap off.

The table A.2 states the mean and variance values for two shutter times of identified erroneous pixels. The figures A.3 and A.4 present histograms of computed mean image.

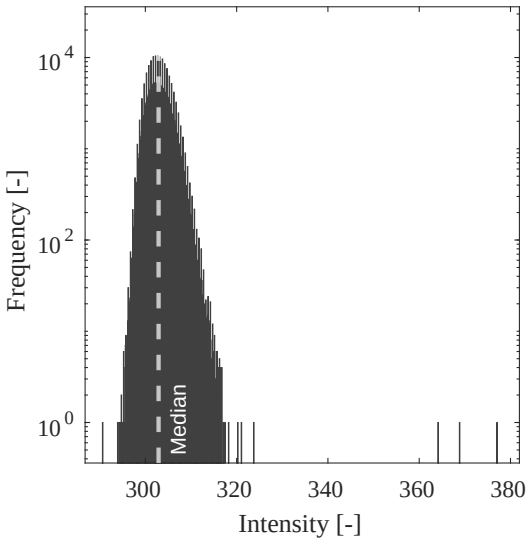

Figure A.3. Histogram of mean image (Fig. 4.9) with camera lens cap off and shutter speed 16.7 ms.

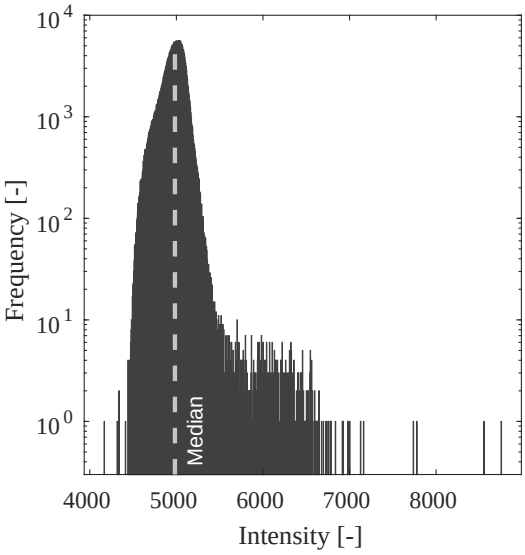

Figure A.4. Histogram of mean image (Fig. 4.10) with camera lens cap off and shutter speed 500 ms.

	16.7 ms				500 ms			
	Lens cap off		Lens cap on		Lens cap off		Lens cap on	
Position	Mean	Variance	Mean	Variance	Mean	Variance	Mean	Variance
[443, 484]	3 215.00	10.37 $\cdot 10^6$	3 222.30	3.25 $\cdot 10^6$	7 124.70	3.68 $\cdot 10^6$	5 632.70	6.22 $\cdot 10^6$
[60, 288]	377.10	122.54	362.30	181.34	5 191.80	29.95	5 169.00	139.56
[381, 300]	364.10	22.10	360.70	12.46	5 891.20	58.84	5 891.00	107.33
[421, 515]	368.90	58.32	362.40	71.82	6 547.00	56.00	6 535.50	120.50
[19, 313]	307.50	60.06	304.50	38.28	5 564.00	7 972.89	5 547.60	13 122.04
[71, 587]	302.90	49.22	298.70	18.01	6 106.40	4 452.04	5 956.30	12 130.90
[351, 633]	295.20	2.18	303.50	106.50	4 797.20	13 769.96	4 870.40	34 668.93
[421, 308]	312.70	41.12	310.80	100.18	6 429.20	1 303.07	6 388.90	3 328.77
[407, 53]	304.20	50.40	305.00	42.89	7 004.70	90.46	6 990.90	212.10
[309, 138]	304.70	77.12	295.60	24.04	8 754.90	146.54	8 747.10	78.99
[487, 246]	305.80	46.18	306.00	42.00	7 779.60	41.82	7 771.90	145.88
[333, 258]	304.60	24.49	305.60	33.38	7 739.50	108.50	7 732.80	75.51
[113, 361]	300.30	10.23	300.80	18.62	7 128.10	126.77	7 118.90	93.21
[53, 544]	305.00	53.11	301.30	22.46	7 161.70	199.34	7 156.80	70.62
[421, 604]	301.80	37.29	301.00	30.89	8 554.00	91.56	8 552.00	154.89

Table A.2. HAMAMATSU C12741-03 (camera two) identified erroneous pixels.

Appendix B
Sensor parameters

This appendix contains a table with an excerpt of sensor parameters used in the camera two in tab B.3. Its block diagram is shown in Fig. B.5. For more information see section 4.1.

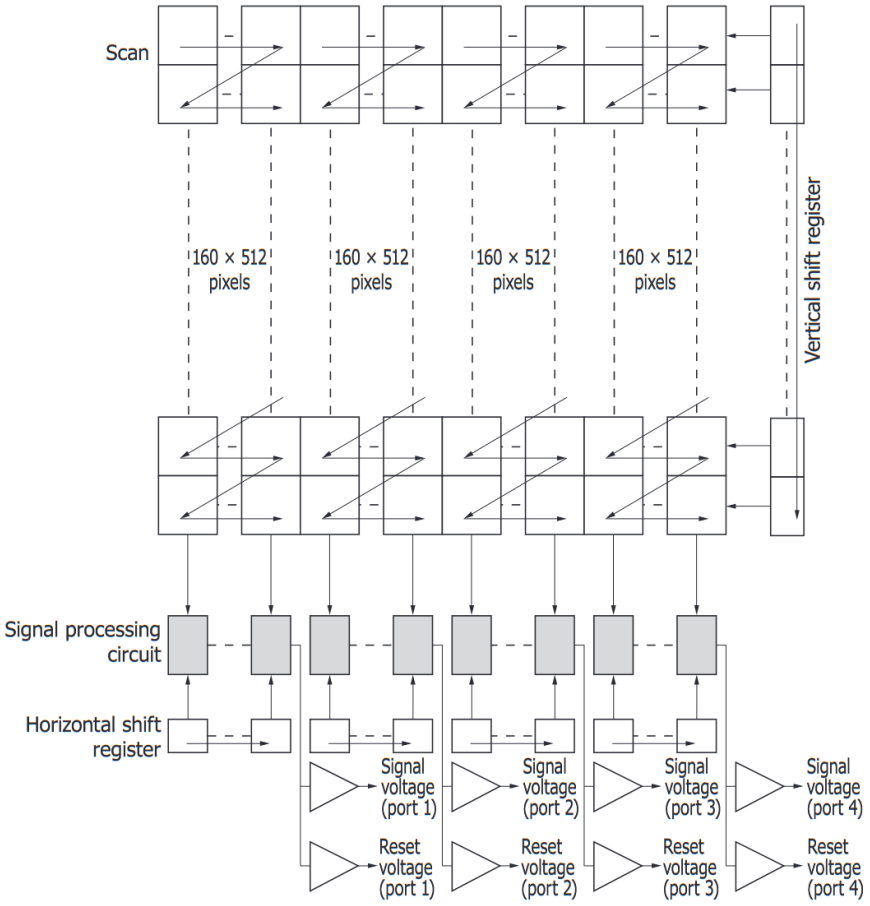

Figure B.5. Block diagram of sensor's chip G13393-0909W. Noticeably, four analog-digital converters are used, each processing area of 160 × 512 pixels.[32]

Parameter	Specification	Units
Effective number of pixels	640 × 512	px
Pixel size	20 × 20	μm
Effective area	12.8 × 10.24	mm
Sensitivity wavelength	950 – 1700	nm
Min exposure time	16.1	ms

Table B.3. Excerpt of HAMAMATSU G13393-0909W sensor parameters (used in camera 2). Full list is accessible from [32].

Appendix C
Experiments

This appendix contains some additional figures and tables for the conducted experiments, described in chapter 5. Fig. C.6 shows unexpected behavior of the laser beam on an intensity profile cut of three sequential images from dataset two taken by camera one. The table C.4 shows statistics for the iterative ABC algorithm on images, in which erroneous pixels were removed. Lastly, table C.5 shows the ground truth parameters of the Gaussian function in the generated dataset D2 and table C.6 shows fitted parameters by the ABC—Ellipse algorithm.

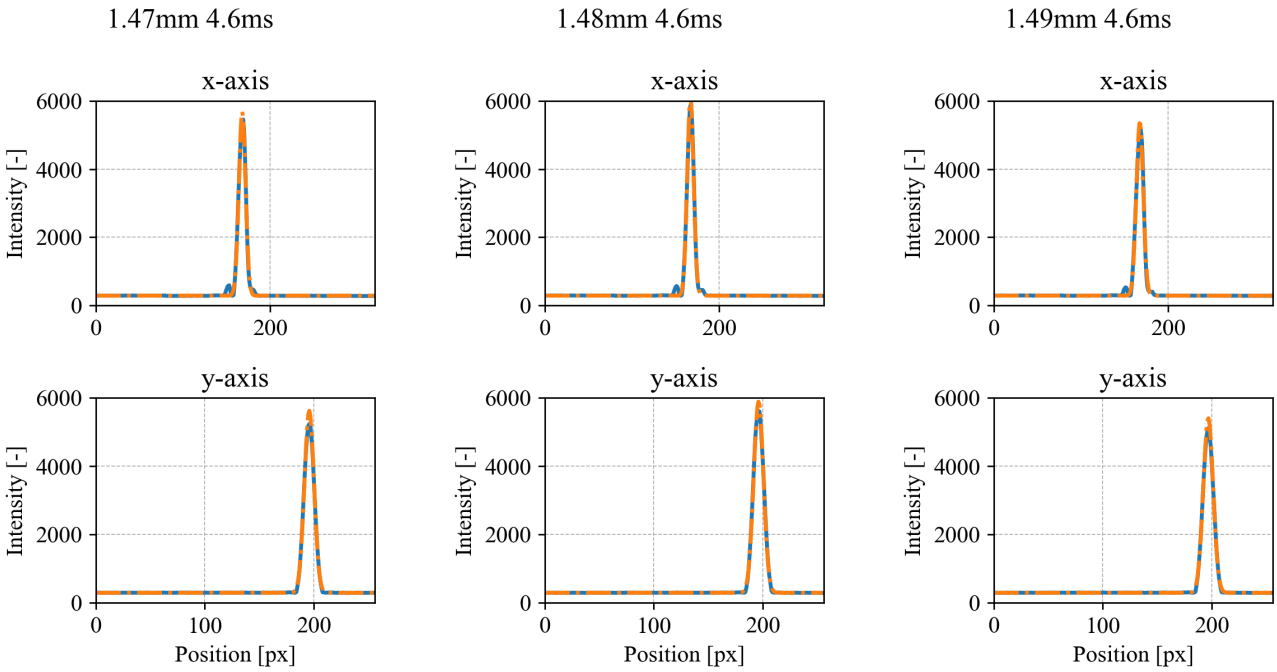

Figure C.6. Axial graph cuts (blue) with fitted Gaussians (orange) for camera positions beyond the focal point. Images taken from dataset B.

		All		Successful	
		Max	Ellipse	Max	Ellipse
No. of Iterations	Mean	13.03	12.54	12.07	12.49
	Q_1	9.50	10.00	8.00	9.00
	Q_2	13.00	12.00	11.00	11.00
	Q_3	16.00	14.00	13.75	14.00
$\bar{r}_i$	Mean	68.23	64.80	35.51	35.51
	Q_1	18.64	18.64	34.10	34.10
	Q_2	38.85	38.85	14.81	14.81
	Q_3	65.87	65.87	42.56	42.56

Table C.4. Impact of different methods for initial parameters on number of LSQ iterations and final error per pixel for ABC algorithm with fixed erroneous pixels before fitting. Q_i represents i-th quartile.

z [mm]	**A** [-]	$\boldsymbol{x_0}$ [px]	$\boldsymbol{y_0}$ [px]	$\boldsymbol{\sigma_x}$ [px]	$\boldsymbol{\sigma_y}$ [px]	$\boldsymbol{\theta}$ [rad]	$\boldsymbol{I_0}$ [-]
0.0	1 600.00	149.00	116.00	20.00	10.00	1.337	304.30
0.1	1 760.00	159.00	126.00	18.86	9.56	1.337	304.30
0.2	2 320.00	169.00	136.00	17.71	9.13	1.337	304.30
0.3	2 720.00	179.00	146.00	16.57	8.69	1.337	304.30
0.4	3 200.00	189.00	156.00	15.43	8.26	1.337	304.30
0.5	3 520.00	199.00	166.00	14.29	7.82	1.337	304.30
0.6	3 840.00	209.00	176.00	13.14	7.39	1.337	304.30
0.7	4 800.00	219.00	186.00	12.00	6.95	1.337	304.30
0.8	6 400.00	229.00	196.00	10.86	6.51	1.337	304.30
0.9	8 160.00	239.00	206.00	9.71	6.08	1.337	304.30
1.0	9 760.00	249.00	216.00	8.57	5.64	1.337	304.30
1.1	11 200.00	259.00	226.00	7.43	5.21	1.337	304.30
1.2	12 800.00	269.00	236.00	6.29	4.77	1.337	304.30
1.3	14 400.00	279.00	246.00	5.14	4.34	1.337	304.30
1.4	16 000.00	289.00	256.00	4.00	3.90	1.337	304.30
1.5	14 400.00	299.00	266.00	4.25	4.15	2.909	304.30
1.6	12 800.00	309.00	276.00	4.50	4.40	2.909	304.30
1.7	11 200.00	319.00	286.00	4.75	4.65	2.909	304.30
1.8	9 600.00	329.00	296.00	5.00	4.90	2.909	304.30
1.9	8 000.00	339.00	306.00	5.25	5.15	2.909	304.30
2.0	6 400.00	349.00	316.00	5.50	5.40	2.909	304.30

Table C.5. Ground truth to Gaussian parameters in the generated dataset D2.

z [mm]	**A** [-]	$\boldsymbol{x_0}$ [px]	$\boldsymbol{y_0}$ [px]	$\boldsymbol{\sigma_x}$ [px]	$\boldsymbol{\sigma_y}$ [px]	$\boldsymbol{\theta}$ [rad]	$\boldsymbol{I_0}$ [-]
0.0	1 600.01	149.00	116.00	20.01	10.00	1.337	304.01
0.1	1 760.00	159.00	126.00	18.86	9.57	1.337	304.01
0.2	2 319.97	169.00	136.00	17.72	9.13	1.337	304.01
0.3	2 720.04	179.00	146.00	16.57	8.69	1.337	304.00
0.4	3 200.01	189.00	156.00	15.43	8.26	1.337	304.00
0.5	3 519.98	199.00	166.00	14.29	7.82	1.337	304.00
0.6	3 839.97	209.00	176.00	13.14	7.39	1.337	304.00
0.7	4 800.03	219.00	186.00	12.00	6.95	1.337	304.00
0.8	6 400.03	229.00	196.00	10.86	6.51	1.337	304.00
0.9	8 160.00	239.00	206.00	9.71	6.08	1.337	304.00
1.0	9 760.03	249.00	216.00	8.57	5.64	1.337	304.00
1.1	11 199.97	259.00	226.00	7.43	5.21	1.337	304.00
1.2	12 800.02	269.00	236.00	6.29	4.77	1.337	304.00
1.3	14 399.93	279.00	246.00	5.14	4.34	1.337	304.00
1.4	16 000.07	289.00	256.00	4.00	3.90	1.337	304.00
1.5	14 399.93	299.00	266.00	4.25	4.15	2.907	304.00
1.6	12 800.06	309.00	276.00	4.50	4.40	2.908	304.00
1.7	11 199.98	319.00	286.00	4.75	4.65	2.908	304.00
1.8	9 600.15	329.00	296.00	5.00	4.90	2.908	304.00
1.9	7 999.93	339.00	306.00	5.25	5.15	2.907	304.00
2.0	6 400.03	349.00	316.00	5.50	5.40	2.908	304.00

Table C.6. Fitted Gaussian parameters in the generated dataset D2.